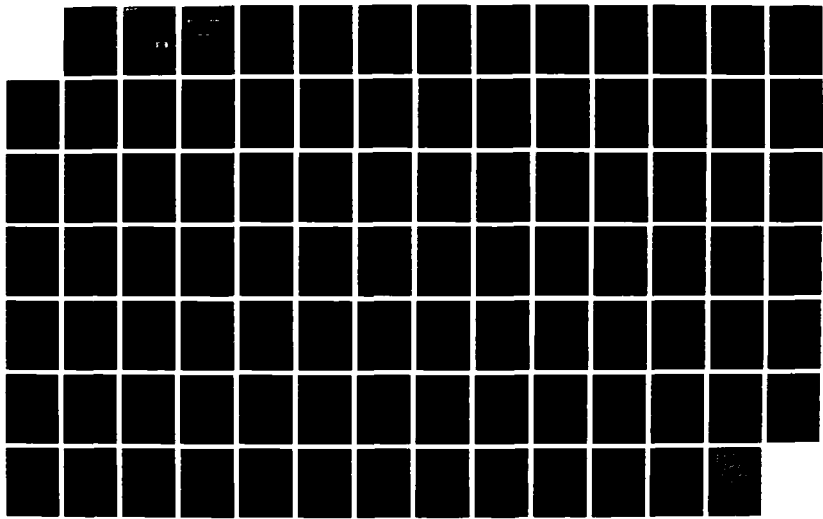
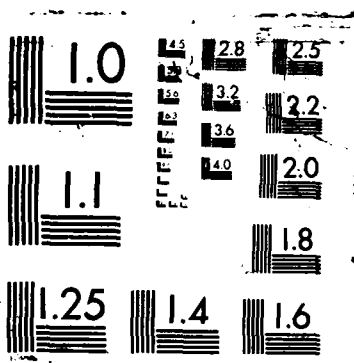


AD-A193 369 DEVELOPMENT OF RADIATION AND CLOUD PARAMETERIZATION  
PROGRAMS FOR AFGL (AI, (U) UTAH UNIV SALT LAKE CITY  
DEPT OF METEOROLOGY S DU ET AL. 86 JAN 88 1/1  
UNCLASIFIED AFGL-TR-88-0018 F19628-83-K-0048 F/G 4/1 NL





FILE COPY

(4)

AD-A193 369

AFGL-TR-88-0018

DEVELOPMENT OF RADIATION AND CLOUD  
PARAMETERIZATION PROGRAMS FOR AFGL  
GLOBAL MODELS

Szu-Cheng Ou  
Kuo-Nan Liou

Center for Atmospheric and Remote Sounding Studies  
Department of Meteorology  
University of Utah  
Salt Lake City, Utah 84112

Final Report  
1 August 1984 - 31 October 1987

DTIC  
SELECTED  
APR 18 1988  
*CJH*  
S D

6 January 1988

Approved for public release; distribution unlimited

AIR FORCE GEOPHYSICS LABORATORY  
AIR FORCE SYSTEMS COMMAND  
UNITED STATES AIR FORCE  
HANSOM AFB, MASSACHUSETTS 01731

88 4 18 061

"This technical report has been reviewed and is approved for publication"

*Samuel Yee*

SAMUEL YEE  
Contract Manager

*Donald A. Chisholm*

DONALD A. CHISHOLM  
Branch Chief

FOR THE COMMANDER

*Robert A. McClatchey*

ROBERT A. MCCLATCHY  
Division Director

This document has been reviewed by the ESD Public Affairs Office (PA) and is releasable to the National Technical Information Service (NTIS).

Qualified requestors may obtain additional copies from the Defense Technical Information Center. All others should apply to the National Technical Information Service.

If your address has changed, or if you wish to be removed from the mailing list, or if the addressee is no longer employed by your organization, please notify AFGL/DAA, Hanscom AFB MA 01731-5000. This will assist us in maintaining a current mailing list.

Do not return copies of this report unless contractual obligations or notices on a specific document requires that it be returned.

## Unclassified

SECURITY CLASSIFICATION OF THIS PAGE (When Data Entered)

REPORT DOCUMENTATION PAGE		READ INSTRUCTIONS BEFORE COMPLETING FORM
1. REPORT NUMBER AFGL-TR-88-0018	2. GOVT ACCESSION NO. A19227	3. RECIPIENT'S CATALOG NUMBER
4. TITLE (and Subtitle) Development of Radiation and Cloud Parameterization Programs for AFGL Global Models	5. TYPE OF REPORT & PERIOD COVERED Final Report 1 August 1984-31 October 1987	
7. AUTHOR(s) Szu-Cheng Ou and Kuo-Nan Liou	6. PERFORMING ORG. REPORT NUMBER F19628-84-K-0040	
9. PERFORMING ORGANIZATION NAME AND ADDRESS Department of Meteorology University of Utah Salt Lake City, Utah 84112	10. PROGRAM ELEMENT, PROJECT, TASK AREA & WORK UNIT NUMBERS 61102F 2310G7AG	
11. CONTROLLING OFFICE NAME AND ADDRESS	12. REPORT DATE 6 January 1988	
	13. NUMBER OF PAGES 92	
14. MONITORING AGENCY NAME & ADDRESS (if different from Controlling Office) Air Force Geophysics Laboratory Hanscom AFB, Massachusetts 01731 Monitor: Samuel Yee/LYP	15. SECURITY CLASS. (of this report) Unclassified 15a. DECLASSIFICATION/DOWNGRADING SCHEDULE	
16. DISTRIBUTION STATEMENT (of this Report) Approved for public release; distribution unlimited.		
17. DISTRIBUTION STATEMENT (of the abstract entered in Block 20, if different from Report)		
18. SUPPLEMENTARY NOTES NA <i>(cc. t)</i>		
19. KEY WORDS (Continue on reverse side if necessary and identify by block number) Infrared radiation; Solar radiation; Radiative transfer; Parameterization; Cloud, University of Utah (UU), General Circulation Model, AFGL variable-resolution model; Cloud formation; Cloud-radiation interaction.		
20. ABSTRACT (Continue on reverse side if necessary and identify by block number) We have devised a computationally economic and accurate radiation program for incorporation in the global models developed at the Air Force Geophysics Laboratory. The program was specifically developed for applications to atmospheres containing high, middle, and low clouds and combinations of these clouds. In addition, we have also developed cloud formation schemes for general circulation models in connection with the radiation program. The present radiation and cloud parameterization program has been successfully		

Unclassified

SECURITY CLASSIFICATION OF THIS PAGE(When Data Entered)

incorporated in the AFGL 12-layer global model. Simulations have been performed for cloud and radiation budget distributions using the initial humidity and temperature fields for 12Z, 17 June 1979. Zonally averaged global distributions of cloud cover and radiation budgets at the top of the atmosphere are in general agreement with available cloud and radiation budget climatologies. Finally, we discuss the importance of clouds in the generation of global atmospheric cooling using the results from the AFGL 12-layer model. (continued) (b) p 6

Accession For	
NTIS GRA&I	<input checked="" type="checkbox"/>
DTIC TAB	<input type="checkbox"/>
Unannounced	<input type="checkbox"/>
Justification	
By _____	
Distribution/ _____	
Availability Codes	
Dist	Avail and/or Special
R-1	



Unclassified  
SECURITY CLASSIFICATION OF THIS PAGE(When Data Entered)

## TABLE OF CONTENTS

	<u>Page</u>
<b>Section 1 INTRODUCTION</b>	1
<b>Section 2 RADIATIVE TRANSFER IN CLEAR ATMOSPHERES</b>	3
<b>2.1 Infrared Radiative Transfer</b>	3
<b>2.2 Solar Radiative Transfer</b>	8
<b>Section 3 RADIATIVE TRANSFER IN MULTILAYERED CLOUDY ATMOSPHERES</b>	13
<b>3.1 Cloud Property Prediction/Prescription</b>	13
<b>3.1.1 Layer Cloud Cover</b>	15
<b>3.1.2 Cloud Strapping Scheme</b>	16
<b>3.1.3 Total Cloud Cover</b>	16
<b>3.2 Parameterization of Radiative Transfer in Cloudy Atmospheres</b>	18
<b>3.2.1 Cloud Configurations</b>	18
<b>3.2.2 IR Flux Exchange</b>	19
<b>3.2.3 Solar Flux Exchange</b>	25
<b>Section 4 INTERCOMPARISON OF RADIATIVE HEATING RATE PROFILES</b>	35
<b>4.1 Intercomparison of Clear-Sky IR Heating Rates</b>	35
<b>4.2 Adding Scheme for Radiative Transfer in Cloudy Atmospheres</b>	36
<b>4.3 Intercomparison of Cloudy-Sky Radiative Heating Rates</b>	42
<b>Section 5 RESULTS OF CLOUD AND RADIATION BUDGET FIELDS</b>	53
<b>5.1 Cloud Prediction</b>	53
<b>5.2 Radiation Budget</b>	53
<b>5.3 Radiative Cooling Rates in the Atmosphere</b>	55
<b>Section 6 SUMMARY</b>	62

	<u>Page</u>
Appendix A SIMPLIFICATION OF RADIATIVE TRANSFER IN HIGH CLOUDS	64
Appendix B DOCUMENTATION OF RADIATION PARAMETERIZATION PROGRAMS	67
B.1 General Description of the Program	67
B.2 Interfacing with the AFGL GCM	69
B.3 Changes Required in the Radiative Routines for Converting Variable Resolution to Fixed Resolution	72
Appendix C DIRECTORY OF ARRAYS AND VARIABLES IN THE RADIATIVE ROUTINES	73
REFERENCES	85

## Section 1

### INTRODUCTION

We have undertaken the development of parameterization programs involving the transfer of thermal IR and solar fluxes in clear and various cloudy atmospheres. The primary objective of this research work is to construct a unified and coherent radiation package that is computationally economic for incorporation into the global models developed at the Air Force Geophysics Laboratory (AFGL). In particular, our major emphasis is on the development of accurate and stable radiation programs for atmospheres containing high, middle, and low clouds and combinations of these clouds. The other objective is to develop cloud formation schemes for the GCM in connection with radiation programs. Our effort in the design of radiation and cloud programs is closely in line with the overall AFGL effort in developing a global model for short and medium range weather prediction and cloud forecast research.

In Section 2 of this report, we describe the physical concepts and basic parameterization equations developed for the computation of radiative fluxes in clear atmospheres. In Section 3 we first present the approaches that are used in predicting and prescribing cloud properties. In particular, the strategy for strapping cloud layers into cloud decks and the method for determining total cloud cover are discussed in some detail. We then present the manner in which the transfer of IR and solar fluxes in multilayered cloudy atmospheres is parameterized. In Section 4, comparisons of IR cooling and solar heating rate profiles for various

cloud configurations computed from the present parameterizations with those from a more exact doubling/adding method, also developed at the University of Utah, are carried out. The present radiation and cloud programs are successfully incorporated in the AFGL 12- and 18-layer models. Simulations are carried out for cloud and radiation fields using the AFGL 12-layer model and initial humidity and temperature fields corresponding to 12Z, 17 June 1979. Results of zonally averaged cloud cover, radiation budgets at the top of the atmosphere and surface, as well as atmospheric cooling profiles generated from the model are presented and discussed in Section 5. Finally, a summary is given in Section 6.

## Section 2

### RADIATIVE TRANSFER IN CLEAR ATMOSPHERES

#### 2.1 Infrared Radiative Transfer

The upward and downward fluxes at a given level in a clear atmosphere in the path length coordinate may be expressed in the forms (Liou, 1980)

$$F^+(u) = \sigma T_s^4 [1 - \epsilon^f(u, T_s)] + \int_0^u \sigma T^4(u') K(u-u') du' , \quad (2.1)$$

$$F^-(u) = \int_{u_1}^u \sigma T^4(u') K(u'-u) du' , \quad (2.2)$$

where  $T_s$  is the surface temperature,  $u$  the path length for the absorbing gas, and  $u_1$  the total path length. The flux expressions in the  $u$ -coordinate can be easily transferred to the height or pressure coordinate. The broadband flux emissivity is defined by

$$\epsilon^f(u, T) = \int_0^\infty \pi B_v(T) [1 - T_v^f(u)] dv / (\sigma T^4) , \quad (2.3)$$

where  $T_v^f$  is the flux transmittance at the spectral wave number  $v$  and  $\pi B_v$  the Planck flux. The kernel function  $K(u-u')$  is related to the broadband flux emissivity as follows:

$$K(u-u') = - \frac{d}{du'} \epsilon^f [|u-u'|, T(u')] . \quad (2.4)$$

To apply the broadband flux emissivity for flux and heating rate

calculations, the IR spectrum is divided into five bands, including (1) H<sub>2</sub>O rotational band, (2) H<sub>2</sub>O continuum band, (3) H<sub>2</sub>O vibrational-rotational band, (4) O<sub>3</sub> rotational-vibrational band, and (5) CO<sub>2</sub> rotational-vibrational band. The overlap between bands (1) and (5) is denoted as band 6. Thus, the broadband flux emissivity may be written in the form

$$\epsilon^f(u, T) = \sum_{i=1}^5 \epsilon_i^f(\tilde{u}_i, T) + \epsilon_6^f(\tilde{u}_w, \tilde{u}_c, T) , \quad (2.5)$$

with the individual broadband flux emissivity defined by

$$\epsilon_i^f = \int_0^\infty \pi B_v(T) [1 - T_{v,i}^f(u)] dv / (\sigma T^4) ,$$

In Eq. (2.5),  $u_1 = u_2 = u_3 = u_w$ , the H<sub>2</sub>O path length,  $u_4 = u_o$ , the O<sub>3</sub> path length,  $u_5 = u_c$ , the CO<sub>2</sub> path length, and  $\tilde{u}_i$  denotes the pressure and temperature corrected path length for the respective absorbing gaseous component. The correction due to overlap is approximated by  $\epsilon_6^f = -\epsilon_1^f(\tilde{u}_w) \epsilon_5^f(\tilde{u}_c)$ .

The broadband emissivities for the four bands may be expressed in terms of polynomial functions in the form (Liou and Ou, 1981)

$$\epsilon_i^f(\tilde{u}_i, T) = \exp \left( \sum_{n=0}^3 c_{ni} \tilde{u}_i^n \right) , \quad (2.6)$$

where

$$\tilde{u}_i = (2 \log_{10} \tilde{u}_i - \bar{a}_i) / \bar{b}_i ,$$

$$\bar{a}_i = \log_{10} (\tilde{u}_{i,max} \cdot \tilde{u}_{i,min}) ,$$

$$\bar{b}_i = \log_{10} (\bar{u}_{i,\max} / \bar{u}_{i,\min}) .$$

The coefficients  $c_{ni}$  were obtained by the least-square method. The quantity  $\bar{u}_i$  is expressed as a linear function of  $\log_{10} \bar{u}_i$ , so that  $-1 < \bar{u}_i < 1$ . Errors are smaller for the intermediate  $\bar{u}_i$  values than for  $\bar{u}_i = -1$  or  $\bar{u}_i = 1$ , due to the characteristic of the least-square method (Hemming, 1973). For water vapor rotational and vibrational-rotational bands, the broadband flux emissivities are derived from the random band parameters assuming the Lorentz line shapes obtained by Rodgers and Walshaw (1966) in which an empirical temperature correction for the rotational band was included. For the water vapor continuum absorption in the window region, the empirical formula developed by Roberts et al. (1976) was used. For ozone, random model parameters for the  $9.6 \mu\text{m}$  band derived by Goldman and Kyle (1968) were utilized to derive the  $O_3$  broadband emissivity. The prescription of  $\bar{u}_{i,\max}$  and  $\bar{u}_{i,\min}$  was according to the range for realistic atmospheres. For water vapor,  $\bar{u}_{i,\max} = 10 \text{ g cm}^{-2}$  and  $\bar{u}_{i,\min} = 10^{-7} \text{ g cm}^{-2}$ . Table 1 lists the coefficients of the broadband emissivity equation  $c_{ni}$  for the three water vapor ( $i = 1, 2, 3$ ) and ozone bands ( $i = 5$ ).

The broadband emissivity for carbon dioxide is computed using the parameterization scheme developed by Ou and Liou (1983). In that paper the  $CO_2$  broadband emissivity, which is a function of the pressure and temperature corrected path length  $\bar{u}_c$  and the atmospheric temperature, is derived from line-by-line transmittance data presented by Fels and Schwarzkopf (1981). From Fig. 1 in the paper by Ou and Liou, the broadband flux emissivity for the  $CO_2$   $15 \mu\text{m}$  band can be fitted into two functional forms:

Table 1. Coefficients of broadband emissivity values for water vapor and ozone bands.

	1	$c_{01}$	$c_{11}$	$c_{21}$	$c_{31}$
T=203°K	1	-.16378+001	.31523+001	-.28231+001	.10998+001
	2	-.98069+001	.91563+001	-.54110+000	-.27859+000
	3	-.58349+001	.54245+001	-.34050+001	.85649-002
	4	-.67785+001	.42930+001	-.95681+000	-.55536+000
T=233°K	1	-.18865+001	.32475+001	-.27705+001	.10903+001
	2	-.95159+001	.91534+001	-.52756+000	-.26671+000
	3	-.50133+001	.53627+001	-.34506+001	.10991-001
	4	-.63805+001	.42918+001	-.95672+000	-.55860+000
T=263°K	1	-.21226+001	.33251+001	-.27277+001	.10832+001
	2	-.93430+001	.91512+001	-.51723+000	-.25749+000
	3	-.44264+001	.53278+001	-.34806+001	.79503-002
	4	-.61317+001	.42910+001	-.95628+000	-.56004+000
T=293°K	1	-.23454+001	.33888+001	-.26927+001	.10777+001
	2	-.92462+001	.91495+001	-.50918+000	-.25017+000
	3	-.39991+001	.53068+001	-.35005+001	.42209-002
	4	-.59797+001	.42904+001	-.95611+000	-.56109+000

$$\epsilon_5^f(\tilde{u}_5, T) = \begin{cases} \exp\left(\sum_{n=0}^3 a_n \tilde{u}_5^n\right), & \text{for } \tilde{u} \geq 10^{-4} \text{ g cm}^{-2} \\ \exp(b_0 + b_1 \tilde{u}_5), & \text{for } \tilde{u} < 10^{-4} \text{ g cm}^{-2} \end{cases}, \quad (2.7)$$

where

$$\tilde{u}' = (2 \log_{10} \tilde{u} + 7.69897)/6.30103 .$$

The coefficient values are  $a_0 = -4.00893 + f(T)$ ,  $a_1 = 4.39828$ ,  $a_2 = -3.07709$ ,  $a_3 = 0.94529$ ,  $b_0 = -4.0036 + f(T)$ , and  $b_1 = 5.13453$ , where

$$f(T) = \ln \{h(T) g(T)/[h(T_0) g(T_0)]\} .$$

The quantities  $h(T)$  and  $g(T)$  are given by

$$h(T) = \frac{1 - T(\tilde{u}_5, T)}{1 - T(\tilde{u}_5, T_0)} = 1 + A\Delta T (1 - B\Delta T) , \quad (2.8)$$

$$g(T) = \int_{v_1}^{v_2} \pi B_v(T) dv / \sigma T^4 , \quad (2.9)$$

where  $T(\tilde{u}_5, T)$  is the transmittance,  $\Delta T = T - T_0$ ,  $A = 1.833 \times 10^{-4}$ ,  $B = 1.364 \times 10^{-2}$ ,  $T_0 = 250^\circ K$ ,  $v_1 = 500 \text{ cm}^{-1}$ , and  $v_2 = 850 \text{ cm}^{-1}$ . Only the coefficients  $a_0$  and  $b_0$  are temperature-dependent since, by using the definition of  $T(\tilde{u}_5, T)$  (Fels and Schwarzkopf, 1981),  $\epsilon^f$  can be expressed by

$$\epsilon^f(\tilde{u}_5, T) = h(T) g(T) [1 - T(\tilde{u}_5, T_0)] . \quad (2.10)$$

In this manner, the dependence of the temperature  $T$  and path length  $\tilde{u}_c$  on the emissivity has been separated.

The pressure and temperature adjustments on the path length for each band are different. For the three water vapor bands, pressure-temperature scaling methods proposed by Liou and Ou (1981) are used.

These are

$$\tilde{u}_1 = \int_0^z \frac{P(z')}{P_0} \exp \{A' [T(z') - T_a] + B' [T(z') - T_a]^2\} \rho_w(z') dz' , \quad (2.11)$$

$$\tilde{u}_2 = \int_0^z \frac{P_w(z')}{P_{0w}} \exp \left\{ - \frac{1800}{T_b T(z')} [T(z') - T_b] \right\} \rho_w(z') dz' , \quad (2.12)$$

$$\bar{u}_3 = \int_0^z \frac{P(z')}{P_0} \left[ \frac{T_c}{T(z')} \right]^{1/2} \rho_w(z') dz' , \quad (2.13)$$

where  $A' = 10.6278 \times 10^{-3} \text{ K}^{-1}$ ,  $B' = -44.6152 \times 10^{-6} \text{ K}^{-2}$ ,  $T_a = 260^\circ\text{K}$ ,  $T_b = 296^\circ\text{K}$ ,  $T_c = 300^\circ\text{K}$ ,  $P_0 = 1013 \text{ mb}$ ,  $\rho_w$  and  $\rho_{ow}$  are vapor pressures at temperatures  $T$  and  $T_b$ , respectively, and  $\rho_w$  is the water vapor density.

The pressure and temperature corrected path lengths for  $\text{CO}_2$  have the form (Ou and Liou, 1983)

$$\bar{u}_5 = 2 c / \{ [1 + 4(c^2/u^2 + c/\bar{u})]^{1/2} - 1 \} , \quad (2.14)$$

where the constant  $c = 3.7551 \times 10^{-4} \text{ g cm}^{-2}$  and

$$\bar{u}_5 = \int_0^z \frac{P(z')}{P_0} \left[ \frac{T_0}{T(z')} \right]^{1/2} \rho_c(z') dz'$$

with  $\rho_c$  the carbon dioxide density and  $T_0 = 273^\circ\text{K}$ . In Eq. (2.14) a combination of  $u$  and  $\bar{u}$  is used, since we were unable to find a single pressure-scaled path length that could provide accurate flux emissivity values. Finally, no adjustment has been made for the ozone path length because of the uncertainty in applying pressure and temperature corrections.

## 2.2 Solar Radiative Transfer

In a clear atmosphere, Rayleigh scattering due to air molecules is insignificant above a height  $z_1$ , about 10 km. The upward solar flux above this height, on the other hand, is contributed from upward Rayleigh reflection plus a diffuse reflection component that results from multiple reflections between the Rayleigh layer and underlying surface. Thus,

the downward and upward solar fluxes at level  $z$  above  $z_1$  may be expressed by

$$F^+(z) = \mu_0 S_0 [1 - A^+(z_T - z)] , \quad (2.15)$$

$$F^+(z) = F^+(z_1) (r_a + G \bar{t}_a) [1 - \bar{A}^+(z - z_1)] , \quad (2.16)$$

where  $z_T$  is the height at the top of the atmosphere, the solar constant  $S_0$  is taken to be  $1360 \text{ W m}^{-2}$ , and the cosine of the solar zenith angle is given by (Liou, 1980)

$$\mu_0 = \sin\theta \sin\delta + \cos\theta \cos\delta \cos\Delta , \quad (2.17)$$

where  $\theta$  is the latitude,  $\delta$  the inclination angle, which is a function of the day of the year, and  $\Delta$  the hour angle. The flux reflection  $r_a$  due to Rayleigh scattering is taken to be  $r_a = 0.28/(1 + 6.43 \mu_0)$  (Lacis and Hansen, 1974). The flux transmission is given by  $t_a = 1 - r_a$ .  $\bar{r}_a$  and  $\bar{t}_a$  are the corresponding diffuse (or global) values that are obtained from integration over the positive  $\mu_0$  values. The direct downward gaseous broadband solar absorptivity  $A^+(z)$  will be defined later and its diffuse value  $\bar{A}^+(z) = A^+ [\eta u(z)]$  where the diffusivity factor  $\eta = 1.66$  for  $H_2O$  and 1.9 for  $O_3$ . The higher diffusivity factor for ozone is chosen to account for Rayleigh scattering effects on the ozone absorption. Based on a simple adding procedure, the multiple reflections involving the Rayleigh scattering layer and the surface having a Lambertian albedo of  $r_s$  are described by a nondimensional upward diffuse component given by

$$G = t_a r_s (1 - \bar{r}_a r_s \cdot \bar{t}_a^2)^{-1} . \quad (2.18)$$

In Eq. (2.16), the  $r_a$  term represents the reflection of the direct downward solar flux, while  $G \bar{t}_a$  denotes the diffuse reflection component. Likewise, downward and upward fluxes at heights below  $z_1$  may be expressed by

$$F^+(z) = \mu_0 S_0 [1 - A^+(z_T - z)] , \quad (2.19)$$

$$F^-(z) = F^+(0) r_s [1 - \bar{A}^-(z)] . \quad (2.20)$$

It should be noted that Rayleigh scattering below  $z_1$  will reduce both upward and downward fluxes by about the same amount since its overlap with gaseous absorption in the near infrared may be neglected. Thus, the net flux and hence the heating rate may be evaluated without the incorporation of Rayleigh scattering.

Three absorbers are considered in the transfer of solar radiation, i.e., water vapor, carbon dioxide, and ozone with the former two gases responsible for absorption in the near infrared region and the latter primarily in the UV region. The overlap of  $H_2O$  and  $O_3$  absorption is insignificant so that the broadband solar absorptivity may be expressed by

$$A(z) = \sum_i A_i (u_o / \mu_0) f_i + \sum_i A_i (u_w / \mu_0) f_i + \epsilon A_5 (u_c / \mu_0) , \quad (2.21)$$

where  $u_o$ ,  $u_w$ , and  $u_c$  represent, respectively, path lengths for  $O_3$ ,  $H_2O$ , and  $CO_2$ , and  $f_i$  are the fractional solar fluxes associated with the individual band absorptivities  $A_i$ . The  $H_2O-CO_2$  overlap correction is given by  $\epsilon = a + b A_5(u_w) \Delta v_5$ , where  $a$  and  $b$  are empirical constants

derived from the measured data presented by Howard et al. (1956);  $a = 0.75$  and  $b = -0.0015$  for  $A_5(u_w) \Delta v_5 \geq 300 \text{ cm}^{-1}$ , and  $a = 1$  and  $b = -0.00233$  for  $A_5(u_w) < 300 \text{ cm}^{-1}$ .

The individual absorptivity for ozone is given by

$$A_1(u_o/\mu_0) = 1 - \exp(-k_1 u_o/\mu_0) , \quad (2.22)$$

where  $k_1$  denote the ozone absorption coefficients taken from the data obtained by Inn and Tanaka (1953) and Vigroux (1953), and  $u_o$  is in units of cm-atm. Table 2 lists the values of the ozone absorption coefficients and fractional solar fluxes.

For water vapor and carbon dioxide, the empirical band equation derived by Liou and Sasamori (1975) is used. It has the following analytic form

$$A_1(u/\mu_0) = \frac{1}{\Delta v_1} \left[ C_1 + D_1 \log_{10} \left( \frac{u}{\mu_0} \bar{P}^{K_1/D_1} + 10^{-C_1/D_1} \right) \right] , \quad (2.23)$$

where  $\Delta v_1$  are the band widths,  $C_1$ ,  $D_1$ , and  $K_1$  are empirical constants. The pressure  $P$  in units of mm Hg is weighted over the path length given by

$$\bar{P} = \int_0^u P(u) du/u ,$$

where  $u$  can be either  $u_w$  or  $u_c$  and is in units of g cm<sup>-2</sup>. The values of  $C_1$ ,  $D_1$ , and  $K_1$  for six  $H_2O$  and the 2.7  $\mu\text{m}$   $CO_2$  bands are listed in Table 3, along with the fractional solar fluxes.

Table 2. Ozone absorption coefficients and fractional solar fluxes.

$\Delta\lambda$ ( $\mu\text{m}$ )	$i$	$k_i$ (-44°C)	$f_i$
0.20-0.21	1	9.8	$1.24 \times 10^{-4}$
0.21-0.22	2	27	$2.97 \times 10^{-4}$
0.22-0.23	3	75	$4.59 \times 10^{-4}$
0.23-0.24	4	164	$4.59 \times 10^{-4}$
0.24-0.25	5	254	$5.14 \times 10^{-4}$
0.25-0.26	6	290	$7.55 \times 10^{-4}$
0.26-0.27	7	241	$1.35 \times 10^{-3}$
0.27-0.28	8	145	$1.59 \times 10^{-3}$
0.28-0.30	9	33.7	$6.46 \times 10^{-3}$
0.30-0.32	10	2.8	$1.01 \times 10^{-2}$
0.32-0.34	11	0.16	$1.50 \times 10^{-2}$
0.34-0.35	12	0.014	$7.95 \times 10^{-3}$
0.45-0.50	13	0.0107	$7.46 \times 10^{-2}$
0.50-0.55	14	0.055	$6.78 \times 10^{-2}$
0.55-0.60	15	0.11	$6.30 \times 10^{-2}$
0.60-0.65	16	0.09	$5.87 \times 10^{-2}$
0.65-0.70	17	0.038	$5.33 \times 10^{-2}$
0.70-0.80	18	0.015	$9.14 \times 10^{-2}$

Table 3. Empirical constants for H<sub>2</sub>O and CO<sub>2</sub> bands and fractional solar fluxes.

$\lambda$ ( $\mu\text{m}$ )	$i$	$C_i$	$D_i$	$K_i$	$\Delta\nu_i$ ( $\text{cm}^{-1}$ )	$f_i$
$\text{H}_2\text{O}$ band						
0.94	1	-135	230	125	1400	0.0760
1.1	2	-292	345	180	1000	0.0528
1.38	3	202	460	198	1500	0.0732
1.87	4	127	232	144	1100	0.0386
2.7	5	337	246	150	1000	0.0242
3.2	6	-144	295	151	540	0.0088
$\text{CO}_2$ band						
2.7	5	-137	77	68	320	0.0073

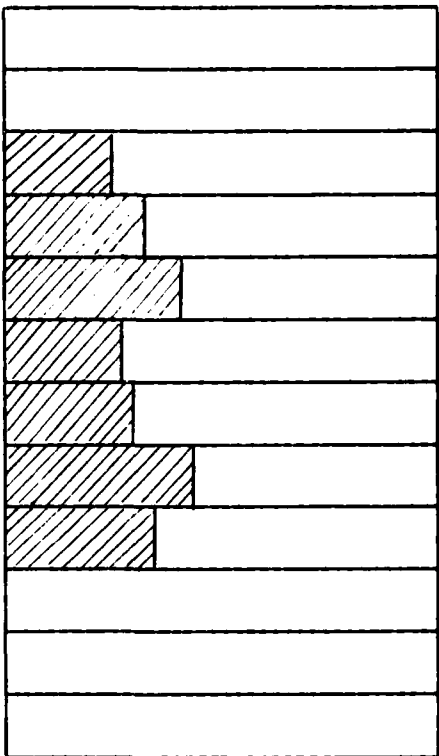
## Section 3

### RADIATIVE TRANSFER IN MULTILAYERED CLOUDY ATMOSPHERES

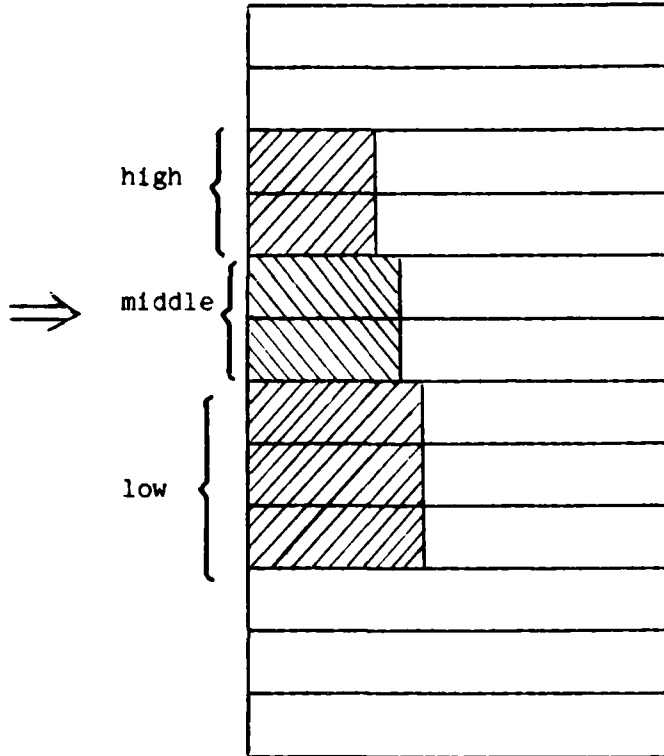
In this section, we shall first present the methods for predicting or prescribing the required cloud properties as input for radiation calculations. We then describe the parameterizations developed for computing both IR and solar flux and heating rate profiles in atmospheres containing multiple stratiform cloud layers.

#### 3.1 Cloud Property Prediction/Prescription

Radiation computations require the cloud top and base heights, cloud cover, and cloud water content as input parameters. In the present radiation model, the vertical structure is the same as that used in the general circulation model (GCM), i.e., both the radiation model and GCM have been modified to accomodate variable resolution. Due to the method used in predicting the layer cloud cover, each model layer has a possibility for cloud formation. We then "strap" two or more contiguous layers into cloud "decks." At present, the model allows at most three decks. In each deck, the cloud is allowed to occupy a fraction of the whole horizontal grid space. In the vertical, however, the cloud is assumed to fill the whole deck domain. Thus, the cloud top is located at the top of the highest model layer in the deck, and the cloud base is at the bottom of the lowest model layer in the deck. This is illustrated in Fig. 1. In the radiation computation, we assume that all cloud decks



(a)



(b)

Fig.1 (a) Partial cloudiness is formed in each model layer. (b) Layer clouds are strapped into three decks of clouds.

occupy the same fraction in the horizontal grid space, and we call this fraction the "total cloud cover." This assumption enables us to save computation time, as the number of vertical integrations for radiation computations is reduced to two in a partially cloudy column. In general, however, the total cloud cover may be determined by certain overlap assumptions. In the remaining part of this subsection, we shall describe the cloud cover prediction method, the strapping of cloud layers, and the assumptions used to determine the total cloud cover. The cloud water content, on the other hand, is prescribed according to typical observed values (e.g., Mason, 1971).

### 3.1.1 Layer Cloud Cover

Most available cloud-cover prediction schemes are diagnostic. They all have similar parameterized forms (Geleyn, 1981; Slingo and Ritter, 1984, etc.):

$$\eta = \begin{cases} \left( \frac{h - h_c}{1 - h_c} \right)^2 & , h > h_c \\ 0 & , h \leq h_c \end{cases} \quad (3.1)$$

But they differ in the prescription of the threshold relative humidity  $h_c$ .

In our present program, we used Geleyn's specification of  $h_c$ , i.e.,

$$h_c = 1 - \alpha\sigma (1-\sigma) [1 + \beta(\sigma-1/2)] , \quad (3.2)$$

where  $\alpha = 2$ ,  $\beta = \sqrt{3}$ ,  $\sigma = p/p_*$ , and  $p_*$  is the surface pressure. In the AFGL 12-layer GCM, clouds are formed in layers 3-9. The top two layers and the bottom three layers are specified as being cloudless.

### 3.1.2 Cloud Strapping Scheme

Based on surface observations, there are generally less than three cloud decks in the vertical. Accordingly, it appears appropriate to strap the model-generated multilayer cloudiness into at most three cloud decks. Since in most GCMs, the vertical structure for both radiation and dynamic programs is fixed, it would be extremely difficult to allow partial cloudiness in the vertical direction. Hence, as we strap the clouds into the cloud deck, it is assumed to fill the respective deck domain vertically. For the AFGL 12-layer GCM, the high, middle, and low cloud decks fill, respectively, layers (3, 4), layers (5, 6), and layers (7, 8, 9). In this manner, the distinction of cloud decks is somewhat arbitrary. Nevertheless, the boundary between high and middle clouds roughly corresponds to the -20°C isotherm, which has been used as a boundary between these clouds by other researchers (e.g., Koenig et al., 1987).

### 3.1.3 Total Cloud Cover

The total cloud cover for each horizontal grid space is determined in two steps. The first step involves calculations of the cloud cover for each deck. Then, the total cloud cover may be evaluated by using certain overlap assumptions. There are two schemes that can be used to determine the cloud deck cover.

#### i) Average Scheme:

The cloud cover for each deck of clouds is the average of the respective cloud cover of model layers. For example, using the AFGL 12-layer model structure, we have

$$\begin{aligned}\eta_h &= \frac{1}{2} (\eta_3 + \eta_4) , \\ \eta_m &= \frac{1}{2} (\eta_5 + \eta_6) , \\ \eta_l &= \frac{1}{3} (\eta_7 + \eta_8 + \eta_9) ,\end{aligned}\quad (3.3)$$

where  $\eta_h$ ,  $\eta_m$ , and  $\eta_l$  denote cloud covers for high, middle, and low clouds.

### ii) Maximum Scheme:

The cloud cover for each deck of cloud is the maximum of the respective cloud cover of model layers. Thus, for the AFGL 12-layer model, we have

$$\begin{aligned}\eta_h &= \max (\eta_3, \eta_4) , \\ \eta_m &= \max (\eta_5, \eta_6) , \\ \eta_l &= \max (\eta_7, \eta_8, \eta_9) .\end{aligned}\quad (3.4)$$

In the present model, we have used the maximum scheme.

To determine the total cloud cover, we must consider the effect of overlap between cloud decks. Several assumptions can be made on the overlap configurations.

### i) Maximum Overlap

In this case, the total cloud cover is given by

$$\eta = \max (\eta_l, \eta_m, \eta_h) .\quad (3.5)$$

### ii) Random Overlap

This configuration assumes that clouds overlap each other in a statistically random manner. Thus, the total cloud cover may be expressed by

$$\eta = 1 - (1 - \eta_l) (1 - \eta_m) (1 - \eta_h) . \quad (3.6)$$

### iii) Minimum Overlap

This configuration assumes that clouds overlap each other in a minimum fashion, so that there are only one-layer cloud configurations, i.e.,

$$\eta = \min (1, \eta_l + \eta_m + \eta_h) . \quad (3.7)$$

It appears reasonable to assume that the cloud configuration in convectively active and overcast regions would tend to be of maximum overlap. In the region of small cloudiness, on the other hand, the cloud configuration would tend to be of minimum overlap.

In the present program, we use the maximum overlap assumption. In each partially cloudy grid space, the total cloud fraction  $\eta = \max (\eta_l, \eta_m, \eta_h)$  and the clear fraction is  $1 - \eta$ . Although each cloud deck has a different cloud cover, for the sake of saving computer time, we set  $\eta_l = \eta_m = \eta_h = \eta$ , whenever  $\eta_l, \eta_m, \eta_h > 0$ .

## 3.2 Parameterization of Radiative Transfer in Cloudy Atmospheres

### 3.2.1 Cloud Configurations

Based on the scheme described previously, there are seven cloud configurations. These include three single-decks, three two-decks, and one three-deck. Using maximum overlap, we first determine the configuration that fits the grid point of interest. Then the cloud cover of each deck is assumed to be the same as the total cloud cover. If the total cloud cover is less than 0.1, the grid is considered to be clear. If, however, the total cloud cover is greater than 0.9, the grid is counted as completely overcast. For the clear and overcast cases, only

one vertical column radiation calculation is necessary. For partially cloudy conditions, two calculations are required.

### 3.2.2 IR Flux Exchange

We consider a three-deck cloud system, as shown in Fig. 2. The high cloud deck is considered to be nonblack. Let the broadband emissivity, transmissivity, and reflectivity for the high cloud deck be denoted by  $\epsilon^c$ ,  $t^c$ , and  $r^c$ , respectively. In a manner similar to that documented in Liou et al. (1984), the flux components for each clear region separated by three decks of clouds may be derived. Above the high cloud we have

$$F^*(z) = \int_{z_T}^z \sigma T^4(z') K(z'-z) dz' , \quad (3.8)$$

$$\begin{aligned} F^*(z) = & \{[r^c F^*(z_{t1}) + t^c F^*(z_{b1}) - (1-\epsilon^c) \sigma T_{t1}^4] \} [1 - \epsilon^f(z-z_{t1}, T_{t1})] \\ & + \sigma T_{t1}^4 [1 - \epsilon^f(z-z_{t1}, T_{t1})] + \int_{z_{t1}}^z \sigma T^4(z') K(z-z') dz' , \end{aligned} \quad (3.9)$$

where  $z_T$  denotes the top height in the model,  $T_{t1}$  the high cloud top temperature, and  $z_{t1}$  and  $z_{b1}$  the high cloud top and base heights, respectively. The expression for the first term on the right-hand side of Eq. (3.9) is explained in Appendix A. Below the high cloud and above the middle cloud we have

$$\begin{aligned} F^*(z) = & [r^c F^*(z_{b1}) + t^c F^*(z_{t1}) - (1-\epsilon^c) \sigma T_{b1}^4] [1 - \epsilon^f(z_{b1}-z, T_{b1})] \\ & + \sigma T_{b1}^4 [1 - \epsilon^f(z_{b1}-z, T_{b1})] + \int_{z_{b1}}^z \sigma T^4(z') K(z'-z) dz , \end{aligned} \quad (3.10)$$

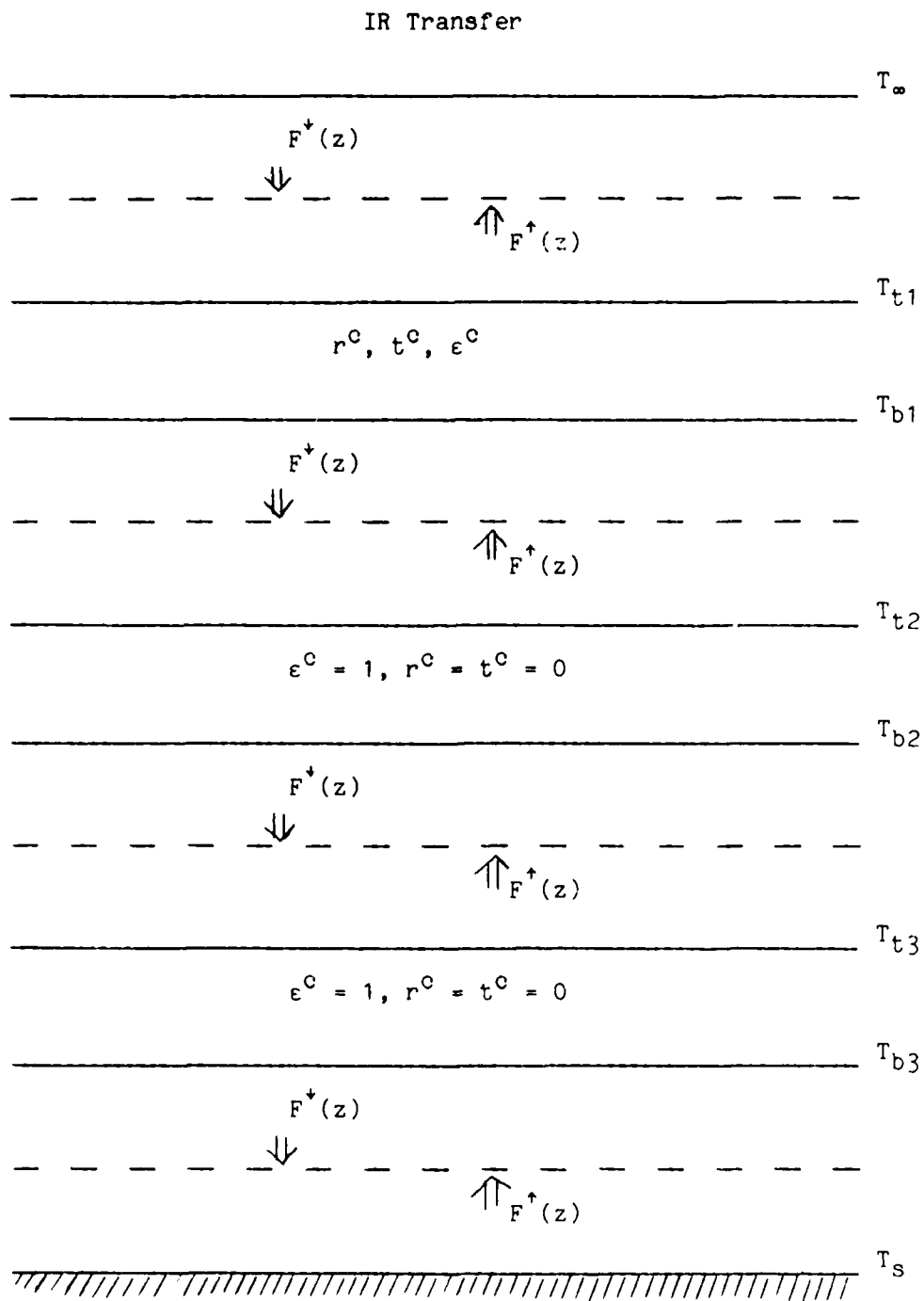


Fig. 2 Geometrical configuration of generalized IR flux transfer in a three-deck cloudy atmosphere.

$$F^*(z) = \sigma T_{t2}^4 [1 - \epsilon^f(z-z_{t2}, T_{t2})] + \int_{z_{t2}}^z \sigma T^4(z') K(z-z') dz' , \quad (3.11)$$

where  $T_{b1}$  is the high cloud base temperature,  $T_{t2}$  the middle cloud top temperature, and  $z_{t2}$  the middle cloud top height. Again, the first term on the right-hand side of Eq. (3.10) is explained in Appendix A. Both middle and low clouds are considered to be blackbodies. Below the middle cloud and above the low cloud we have

$$F^*(z) = \sigma T_{b2}^4 [1 - \epsilon^f(z_{b2}-z, T_{b2})] + \int_{z_{b2}}^z \sigma T^4(z') K(z-z') dz' , \quad (3.12)$$

$$F^*(z) = \sigma T_{t3}^4 [1 - \epsilon^f(z-z_{t3}, T_{t3})] + \int_{z_{t3}}^z \sigma T^4(z') K(z-z') dz' , \quad (3.13)$$

where  $T_{b2}$  is the middle cloud base temperature,  $T_{t3}$  the low cloud top temperature,  $z_{b2}$  the middle cloud base height, and  $z_{t3}$  the low cloud top height. Below the low cloud and above the surface we have

$$F^*(z) = \sigma T_{b3}^4 [1 - \epsilon^f(z_{b3}-z, T_{b3})] + \int_{z_{b3}}^z \sigma T^4(z') K(z-z') dz' , \quad (3.14)$$

$$F^*(z) = \sigma T_s^4 [1 - \epsilon^f(z, T_s)] + \int_0^z \sigma T^4(z') K(z-z') dz' , \quad (3.15)$$

where  $T_{b3}$  is the low cloud base temperature,  $T_s$  the surface temperature, and  $z_{b3}$  the low cloud base height.

When there is only one cloud deck generated in the model, it can be either high (nonblack), middle (black), or low (black). If the cloud is

nonblack, we set  $z_{t2} = 0$ , and  $T_{t2} = T_s$ , and use Eqs. (3.8)-(3.11) only. If the cloud is black, we use Eqs. (3.8)-(3.11) with  $r^c = 0$ ,  $\epsilon^c = 1$ ,  $z_{t2} = 0$ , and  $T_{t2} = T_s$ . When there are two cloud decks generated in the model, the upper deck can be either high (nonblack) or black. In the case of a high cloud on top of a black cloud, we set  $z_{t3} = 0$  and  $T_{t3} = T_s$ , and use Eqs. (3.8)-(3.11). In the case of two decks of black clouds, we use Eqs. (3.8)-(3.13) with  $r^c = 0$ ,  $\epsilon^c = 1$ ,  $z_{t3} = 0$ , and  $T_{t3} = T_s$ . Furthermore, if all three decks of clouds are present in the model, the entire set of Eqs. (3.8)-(3.15) is used in the IR flux calculation.

The flow diagram illustrating the strategy for distinguishing between clear, one-, two-, and three-deck cloudy atmospheres is shown in Fig. 3. The integral quantities  $LC(1)$ ,  $LC(3)$ , and  $LC(5)$  denote the cloud top level indices corresponding to cloud decks one, two, and three, respectively. On the other hand,  $LC(2)$  denotes the cloud base level index for cloud deck one, and  $LCTOP$  and  $LCBOT$  represent the high cloud top and base level index, respectively. We set  $LC(1)$ ,  $LC(3)$ , and  $LC(5)$  to zero whenever the cloud deck is absent. The preceding array elements then become the discriminator for determining the number and type of cloud decks present.

The broadband infrared emissivity, reflectivity, and transmissivity for high clouds are functions of the vertical cloud liquid water content following the parameterization equation developed by Liou and Wittman (1979) in the form

$$R(W) = \sum_{i=0}^{5} c_i W^i , \quad (3.16)$$

where  $R(W)$  denotes the flux reflectivity, transmissivity, or emissivity

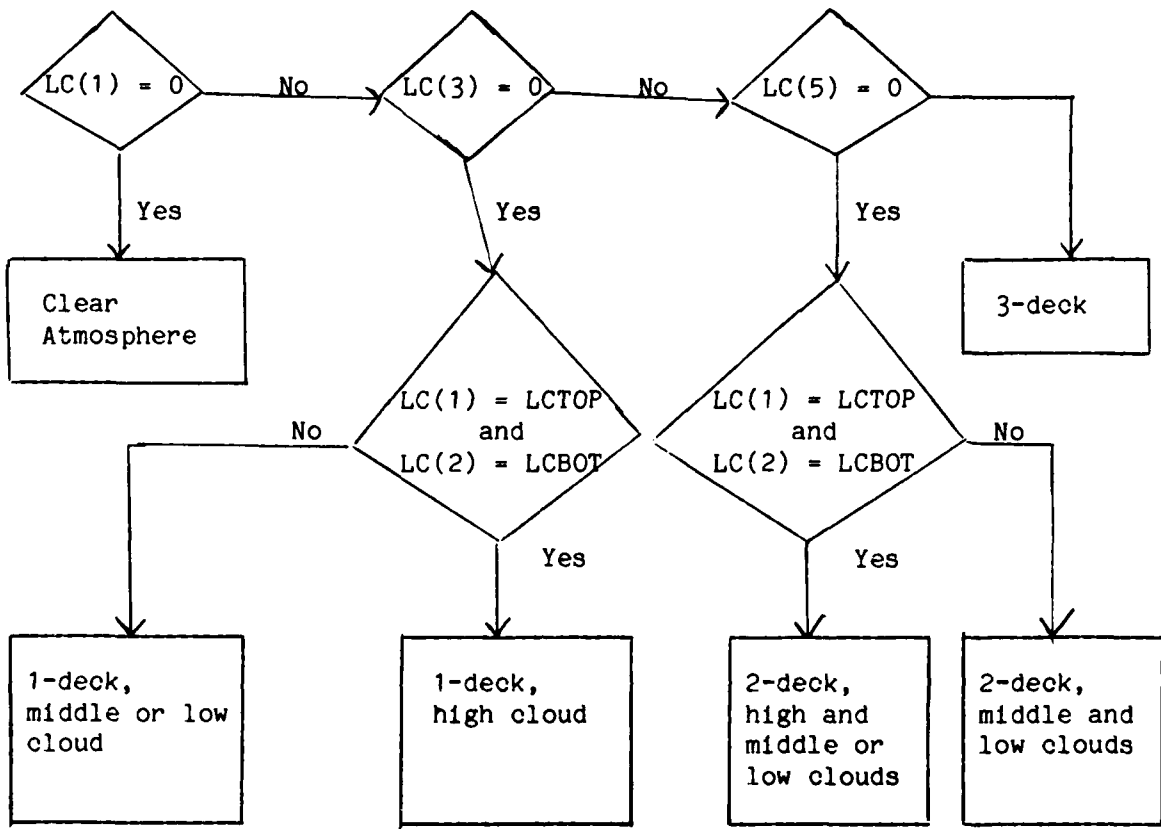


Fig. 3 The flow diagram depicting the strategy for distinguishing between clear, one-, two-, and three-deck cloudy atmospheres. The integral quantities  $LC(1)$ ,  $LC(3)$ , and  $LC(5)$  are the cloud top level indices, which are set to zero if there is no cloud, whereas the parameters  $LCTOP$  and  $LCBOT$  are the high cloud top and base level indices.

Table 4. Predictor coefficients  $c_1$  for high clouds in the infrared region.

i	Reflectivity	Transmissivity	Emissivity
0	0.30619E-01	0.73597E+00	0.28568E+00
1	0.81134E+00	-0.38162E+01	0.35222E+01
2	-0.18995E+01	0.83288E+01	-0.76275E+01
3	0.24900E+01	-0.91066E+01	0.83096E+01
4	-0.15805E+01	0.48765E+01	-0.44405E+01
5	0.37581E+00	-0.10141E+01	0.92209E+00

of the cirrus cloud,  $c_1$  the predictor coefficients, and  $W$  the vertical cloud liquid water content in units of  $10^2 \text{ g m}^{-2}$ . The values of  $c_1$  are listed in Table 4.

For partly cloudy conditions, the infrared cooling rate at each model layer is obtained by linearly weighting the percentages of the total cloud cover  $\eta$  and clear portion  $(1 - \eta)$  in the form

$$\left[ \frac{\partial T}{\partial t} \right]^{pc} = \eta \left[ \frac{\partial T}{\partial t} \right]^c + (1 - \eta) \left[ \frac{\partial T}{\partial t} \right]^{nc}, \quad (3.17)$$

where the superscripts pc, c, and nc represent partly cloudy, cloudy, and clear (no cloud) cases, respectively. This equation is also applicable to solar heating rate calculations under partly cloudy conditions.

The radiative heating rate at level  $z$  is related to the divergence of net fluxes and is given by

$$\frac{\partial T}{\partial t} = - \frac{1}{\rho C_p \Delta z} \Delta [F^+(z) - F^-(z)], \quad (3.18)$$

where  $\rho$  is the air density,  $C_p$  the specific heat at constant pressure,

and  $\Delta z$  the model layer thickness. Equation (3.18) is only applicable to the cloudless region. To compute the heating rate within clouds, two methods are employed. For low and middle black clouds, an approximation method has been developed. The net flux at the model level within the cloud deck may be evaluated by the difference between upward blackbody emission from the lower layer and downward blackbody emission from the upper layer, viz.,

$$F(z) = \sigma T^4(z - \Delta z/2) - \sigma T^4(z + \Delta z/2) . \quad (3.19)$$

Since  $T(z - \Delta z/2) > T(z + \Delta z/2)$ ,  $F(z)$  is always positive. Near the cloud top, since  $F(z_t) = \sigma T^4(z_t - \Delta z/2) - F^+(z_t)$ , and  $F^+(z_t) \ll \sigma T^4(z_t + \Delta z/2)$ ,  $F(z_t) \gg F(z_t - \Delta z)$ , implying a strong cooling there, while near the cloud base,  $F(z_b) > F(z_b + \Delta z)$ , heating is implied. A comparison of the resulting intracloud cooling rate computed from this approximation with that obtained from a more detailed radiative transfer model developed by Kinne (1987) will be shown in a later section. For high clouds, due to their nonblack character, the above approximation cannot be applied. We determine the intracloud flux profile for high clouds by exponential interpolation between cloud top and base fluxes.

### 3.2.3 Solar Flux Exchange

In our previous solar radiation program, calculations could only be performed for one- and two-deck cloudy atmospheres. We have expanded and modified the program to accomodate the computation of flux exchanges in a three-deck cloudy atmosphere. Referring to Fig. 4, we denote the flux reflectivity and transmissivity for the high (1), middle (2), and low (3) clouds as  $(r_1, t_1)$ ,  $(r_2, t_2)$  and  $(r_3, t_3)$ , respectively. The associated

diffuse quantities are defined by

$$\begin{bmatrix} \bar{r} \\ \bar{t} \end{bmatrix} = 2 \int_0^1 \begin{bmatrix} r(u_0) \\ t(u_0) \end{bmatrix} u_0 \, du_0 . \quad (3.20)$$

Moreover, the gaseous transmissivities,  $T_0$ ,  $T_1$ ,  $T_2$ , and  $T_3$  for respective separate clear regions are defined by

$$\begin{bmatrix} T_0 \\ T_1 \\ T_2 \\ T_3 \end{bmatrix} = \begin{bmatrix} 1 - A_0 \\ 1 - A_1 \\ 1 - A_2 \\ 1 - A_3 \end{bmatrix} , \quad (3.21)$$

where the subscripts 0, 1, 2, and 3 represent regions above the high cloud, between high and middle clouds, between middle and low clouds, and below the low cloud, respectively. The quantities  $A_0$ ,  $A_1$ ,  $A_2$ , and  $A_3$  are the total absorptivities of the respective regions. Moreover, we define the multiple reflection factor  $S_{ij}$  as the gain for either the upward or downward flux component due to multiple reflections between the base of the  $i$ th cloud and top of the  $j$ th cloud (or surface). There are three multiple reflection factors, which may be expressed in the forms

$$\begin{bmatrix} \bar{s}_{12} \\ \bar{s}_{23} \\ \bar{s}_{34} \end{bmatrix} = \begin{bmatrix} (1 - \bar{T}_1^{+2} \bar{r}_1 \bar{r}_2)^{-1} \\ (1 - \bar{T}_2^{+2} \bar{r}_2 \bar{r}_3)^{-1} \\ (1 - \bar{T}_3^{+2} \bar{r}_3 r_s)^{-1} \end{bmatrix} , \quad (3.22)$$

where the superscript + signifies transmission of upward propagating radiation, and  $r_s$  is the surface albedo. The over bars denote diffuse quantities. With these definitions, we then define the generating

function,  $G_1$ , the fractional flux based on the incoming solar radiation leaving the cloud boundaries (or surface) in region 1. Referring to Fig. 4, there are three generation functions in each region separated by clouds, namely, the downward direct component  $G^{\downarrow}$ , upward diffuse component  $\bar{G}^{\uparrow}$ , and downward diffuse component  $\bar{G}^{\downarrow}$ . Starting from the model top, we first determine the expression for  $G^{\downarrow}$  in each region. Above the high cloud we have

$$G_1^{\downarrow} = 1 , \quad (3.23)$$

Between high and middle clouds,  $G_2^{\downarrow}$  is the product of the high cloud transmissivity and gaseous transmittance above the high cloud:

$$G_2^{\downarrow} = T_0^{\downarrow} t_1 . \quad (3.24)$$

Between middle and low clouds,  $G_3^{\downarrow}$  is the product of  $G_1^{\downarrow}$ , the gaseous transmittance above the middle cloud, and the middle cloud transmittance:

$$G_3^{\downarrow} = G_1^{\downarrow} T_1^{\downarrow} t_2 , \quad (3.25)$$

Below the low cloud,  $G_4^{\downarrow}$  is the product of  $G_3^{\downarrow}$ , the gaseous transmittance above the low cloud, and the low cloud transmittance:

$$G_4^{\downarrow} = G_3^{\downarrow} T_2^{\downarrow} t_3 , \quad (3.26)$$

After  $G^{\downarrow}$  has been defined, we may derive expressions for  $\bar{G}^{\uparrow}$ . Above the high cloud,  $\bar{G}_1^{\uparrow}$  is composed of two components, due to (1) reflection of the direct downward flux at the cloud top 1, and (2) transmission of the diffuse upward flux  $\bar{G}_2^{\uparrow}$  through cloud 1. Thus,

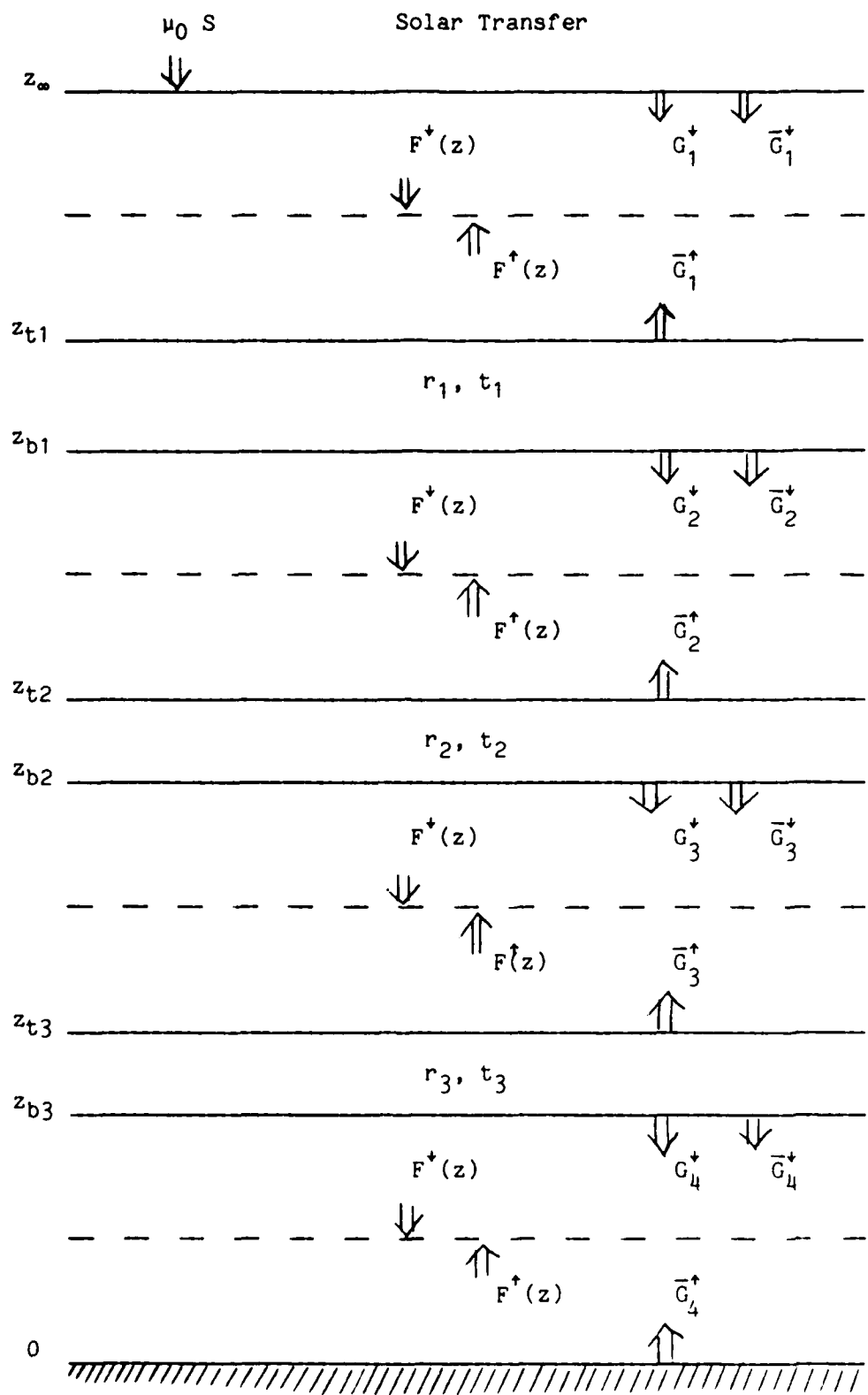


Fig. 4 Geometrical configuration of generalized solar flux transfer in a three-deck cloudy atmosphere.

$$\bar{G}_1^+ = G_1^+ T_0^+ r_1 + \bar{G}_2^+ \bar{T}_1^+ \bar{t}_1 . \quad (3.27)$$

The function  $\bar{G}_2^+$  is also composed of two components involving multiple reflections of the direct downward flux, and transmission of the diffuse upward flux  $\bar{G}_3^+$  through cloud 2. Thus,

$$\bar{G}_2^+ = G_2^+ T_1^+ r_2 \bar{s}_{12} + \bar{G}_3^+ \bar{T}_2^+ \bar{t}_2 . \quad (3.28)$$

The function  $\bar{G}_3^+$  is composed of three components. These are multiple reflections of direct and diffuse downward fluxes, and upward transmission of the diffuse upward flux  $\bar{G}_4^+$  through cloud 3. Thus, we write

$$\bar{G}_3^+ = (G_3^+ T_2^+ r_3 + \bar{G}_2^+ \bar{T}_1^+ \bar{t}_2 \bar{T}_2^+ \bar{r}_3) \bar{s}_{23} + \bar{G}_4^+ \bar{T}_3^+ \bar{t}_3 . \quad (3.29)$$

The function  $\bar{G}_4^+$  is composed of two components associated with multiple reflections of direct and diffuse downward fluxes at the surface, that is,

$$\bar{G}_4^+ = (G_4^+ T_3^+ + \bar{G}_3^+ \bar{T}_2^+ \bar{t}_3 \bar{T}_3^+) r_s \bar{s}_{34} . \quad (3.30)$$

The expressions for the downward diffuse function  $\bar{G}^+$  may be derived in a similar manner. At the model top, there is no downward diffuse radiation, so that

$$\bar{G}_1^+ = 0 . \quad (3.31)$$

Further downward,  $\bar{G}_2^+$  may be expressed as the reflected amount of the upward diffuse flux in the form

$$\bar{G}_2^+ = \bar{G}_2^+ \bar{T}_1^+ \bar{r}_1 . \quad (3.32)$$

Subsequently,  $\bar{G}_3^\downarrow$  and  $\bar{G}_4^\downarrow$  may be written as the sum of the reflected amount of both diffuse upward and diffuse downward fluxes in the forms

$$\bar{G}_3^\downarrow = \bar{G}_3^\uparrow \bar{T}_2^\uparrow \bar{r}_2 + \bar{G}_2^\downarrow \bar{T}_1^\downarrow \bar{t}_2 , \quad (3.33)$$

$$\bar{G}_4^\downarrow = \bar{G}_4^\uparrow \bar{T}_3^\uparrow \bar{r}_3 + \bar{G}_3^\downarrow \bar{T}_2^\downarrow \bar{t}_3 . \quad (3.34)$$

The G functions relevant to direct downward transmission, i.e.,  $G_1^\downarrow$ ,  $G_2^\downarrow$ ,  $G_3^\downarrow$ , and  $G_4^\downarrow$ , involve known quantities of cloud and gaseous absorption. They can be successively computed explicitly in the order of  $G_1^\downarrow \rightarrow G_2^\downarrow \rightarrow G_3^\downarrow \rightarrow G_4^\downarrow$ . The rest of the G functions are interrelated. By substituting Eq. (3.28) into Eq. (3.32), we obtain  $\bar{G}_2^\downarrow$  as a function of  $\bar{G}_3^\uparrow$ :

$$\bar{G}_2^\downarrow = (G_2^\downarrow T_1^\downarrow r_2 \bar{s}_{12} + \bar{G}_3^\uparrow \bar{T}_2^\uparrow \bar{t}_2) \bar{T}_1^\uparrow \bar{r}_1 . \quad (3.35)$$

Moreover, substituting Eq. (3.35) into Eq. (3.30), leads to an expression relating  $\bar{G}_4^\downarrow$  as a function of  $\bar{G}_3^\uparrow$  in the form

$$\begin{aligned} \bar{G}_4^\downarrow = & [G_4^\downarrow T_3^\downarrow + (G_1^\downarrow T_1^\downarrow r_2 \bar{s}_{12} + \bar{G}_3^\uparrow \bar{T}_2^\uparrow \bar{t}_2) \bar{T}_1^\uparrow \bar{r}_1 \\ & \cdot \bar{T}_1^\downarrow \bar{t}_3 \bar{T}_3^\downarrow] r_s \bar{s}_{34} . \end{aligned} \quad (3.36)$$

Finally, we substitute both Eqs. (3.35) and (3.36) into Eq. (3.29), and solve for  $\bar{G}_3^\uparrow$  to obtain

$$\bar{G}_3^\uparrow = (y_1 + y_2 + y_3 + y_4) / (1 - x_1 - x_2) , \quad (3.37)$$

where

$$y_1 = G_3^\downarrow T_2^\downarrow r_3 \bar{s}_{23} , \quad (3.38)$$

$$y_2 = G_2^+ T_1^+ r_2 \bar{s}_{12} \bar{T}_1^+ \bar{r}_1 \bar{T}_1^+ \bar{t}_2 \bar{T}_2^+ \bar{r}_3 \bar{s}_{23} , \quad (3.39)$$

$$y_3 = G_4^+ T_3^+ r_s \bar{s}_{34} \bar{T}_3^+ \bar{t}_3 , \quad (3.40)$$

$$y_4 = G_2^+ T_1^+ r_2 \bar{s}_{12} \bar{T}_1^+ \bar{r}_1 \bar{T}_1^+ \bar{t}_2 \bar{T}_2^+ \bar{t}_3 \bar{T}_3^+ r_s \bar{s}_{34} \bar{T}_3^+ \bar{t}_3 , \quad (3.41)$$

$$x_1 = \bar{T}_2^+ \bar{t}_2 \bar{T}_1^+ \bar{r}_1 \bar{T}_1^+ \bar{t}_2 \bar{T}_2^+ \bar{r}_3 \bar{s}_{23} , \quad (3.42)$$

$$x_2 = (\bar{T}_2^+ \bar{r}_2 + \bar{T}_2^+ \bar{t}_2 \bar{T}_1^+ \bar{r}_1 \bar{T}_1^+ \bar{t}_2) \bar{T}_2^+ \bar{t}_3 \bar{T}_3^+ r_s \bar{s}_{34} \bar{T}_3^+ \bar{t}_3 . \quad (3.43)$$

The remaining G functions may be computed according to Eqs. (3.27)-(3.34) in the order  $\bar{G}_2^+ \rightarrow \bar{G}_1^+ \rightarrow \bar{G}_2^+ \rightarrow \bar{G}_3^+ \rightarrow \bar{G}_4^+ \rightarrow \bar{G}_4^+$ .

Using the preceding G functions, we can compute the flux components for each clear region separated by cloud decks. Above the high cloud we have

$$F^+(z) = \mu_0 S_0 G_1^+ [1 - A^+(z_T - z)] , \quad (3.44)$$

$$F^+(z) = \mu_0 S_0 \bar{G}_1^+ [1 - \bar{A}^+(z - z_{t1})] . \quad (3.45)$$

where  $S_0$  denotes the solar constant, and  $\mu_0$  the cosine of the solar zenith angle. Between the high and middle clouds, we find

$$F^+(z) = \mu_0 S_0 \{ G_2^+ [1 - A^+(z_{b1} - z)] + \bar{G}_2^+ [1 - \bar{A}^+(z_{b1} - z)] \} , \quad (3.46)$$

$$F^+(z) = \mu_0 S_0 \bar{G}_2^+ [1 - \bar{A}^+(z - z_{t2})] . \quad (3.47)$$

Between the middle and low clouds, we have

$$F^*(z) = \mu_0 S_0 \{G_3^* [1 - A^*(z_{b2}-z)] + \bar{G}_3^* [1 - \bar{A}^*(z_{b2}-z)]\} , \quad (3.48)$$

$$F^*(z) = \mu_0 S_0 \bar{G}_3^* [1 - \bar{A}^*(z-z_{t3})] . \quad (3.49)$$

And below the low cloud, we find

$$F^*(z) = \mu_0 S_0 \{G_4^* [1 - A^*(z_{b3}-z)] + \bar{G}_4^* [1 - \bar{A}^*(z_{b3}-z)]\} , \quad (3.50)$$

$$F^*(z) = \mu_0 S_0 \bar{G}_4^* [1 - \bar{A}^*(z)] . \quad (3.51)$$

The broadband solar reflection and transmission values for various cloud decks are obtained through the following parameterization equation based on detailed radiative transfer calculations:

$$r,t(\mu_0, w) = \sum_{m=0}^3 \sum_{n=0}^3 b_{mn} \mu_0^m w^n , \quad (3.52)$$

where  $b_{mn}$  are empirical coefficients derived from the parameterization principle proposed by Liou and Wittman (1979), and the vertical liquid water content  $w$  is in units of  $10^2 \text{ g m}^{-2}$ . The  $b_{mn}$  for Cu (low cloud), As (middle cloud), and Ci (high cloud) are given in Tables 5, 6, and 7, respectively. Computations of solar heating rates in clear, overcast, and partly cloudy conditions follow Eqs. (3.17) and (3.18). However, to compute intracloud heating rates, we use an exponential interpolation of fluxes at the cloud top and base. Results will be presented in the next section.

Table 5. Approximating predictor coefficients  $b_{ij}$  for Cu (low cloud).

i	j			
	0	1	2	
Reflection				
0	0.51771E+00	0.18277E+00	-0.35851E-01	0.23478E-02
1	0.72387E+00	-0.27019E+00	0.51303E-01	-0.34428E-02
2	-0.21499E+01	0.75225E+00	-0.14588E+00	0.97306E-02
3	0.12157E+01	-0.40120E+00	0.78145E-01	-0.52224E-02
Transmission				
0	0.43642E+00	-0.22727E+00	0.44702E-01	-0.29117E-02
1	-0.66319E+00	0.35415E+00	-0.70708E-01	0.46403E-02
2	0.19014E+01	-0.10256E+01	0.20574E+00	-0.13534E-01
3	-0.10157E+01	0.54533E+00	-0.10912E+00	0.71667E-02
Absorption				
0	0.66103E-01	0.34702E-01	-0.69662E-02	0.44253E-03
1	-0.79484E-01	-0.73614E-01	0.17572E-01	-0.10799E-02
2	0.29293E+00	0.25047E+00	-0.55398E-01	0.35139E-02
3	-0.22077E+00	-0.13272E+00	0.28740E-01	-0.17990E-02

Table 6. Approximating predictor coefficients  $b_{ij}$  for As (middle cloud).

i	j			
	0	1	2	
Reflection				
0	0.64457E+00	0.28785E+00	-0.12069E+00	0.16673E-01
1	0.44388E+00	-0.45496E+00	0.18695E+00	-0.26672E-01
2	-0.14875E+01	0.13141E+01	-0.54825E+00	0.77121E-01
3	0.85585E+00	-0.71346E+00	0.29823E+00	-0.41922E-01
Transmission				
0	0.30735E+00	-0.35373E+00	0.14797E+00	-0.20208E-01
1	-0.44042E+00	0.50188E+00	-0.20975E+00	0.28630E-01
2	0.13537E+01	-0.15738E+01	0.66248E+00	-0.90739E-01
3	-0.73396E+00	0.85256E+00	-0.35858E+00	0.49077E-01
Absorption				
0	0.70594E-01	0.40901E-01	-0.16982E-01	0.21345E-02
1	-0.28640E-01	-0.18917E-01	0.11167E-01	-0.37025E-03
2	0.19500E+00	0.19298E+00	-0.86520E-01	0.98269E-02
3	-0.15133E+00	-0.10728E+00	0.47143E-01	-0.53524E-02

Table 7. Approximating predictor coefficients  $b_{1j}$  for  $C_1$  (high cloud).

i	j			
	0	1	2	3
Reflection				
0	0.25264E+00	0.45462E+00	-0.29492E+00	0.82536E-01
1	-0.29273E+00	0.22029E+01	-0.24834E+01	0.82674E+00
2	-0.24531E+00	-0.63610E+01	0.75864E+01	-0.25896E+01
3	0.35097E+00	0.38933E+01	-0.49188E+01	0.17187E+01
Transmission				
0	0.78722E+00	-0.66348E+00	0.44495E+00	-0.12500E+00
1	0.73255E+00	-0.43772E+01	0.47094E+01	-0.15549E+01
2	-0.68508E+00	0.11764E+02	-0.13716E+02	0.46796E+01
3	0.15453E+00	-0.70865E+01	0.87472E+01	-0.30566E+01
Absorption				
0	0.49388E-01	0.13715E+00	-0.10122E+00	0.28402E-01
1	-0.19622E+00	0.11882E+01	-0.12267E+01	0.40299E+00
2	0.24118E+00	-0.23149E+01	0.28776E+01	-0.10168E+01
3	-0.94420E-01	0.11305E+01	-0.15772E+01	0.58577E+00

## Section 4

### INTERCOMPARISON OF RADIATIVE HEATING RATE PROFILES

In this section, we present heating rate results for clear and various cloudy atmospheres.

#### 4.1 Intercomparison of Clear-Sky IR Heating Rates

Using the IR radiative transfer parameterization described in Section 2, we have carried out a number of numerical comparisons and verifications with more detailed band model and/or line-by-line calculations (Liou and Ou, 1981; Ou and Liou, 1983). Specifically, we have computed cooling rates due to H<sub>2</sub>O and O<sub>3</sub> emission, in a tropical atmosphere and compared them with results from a band model developed by Roewe and Liou (1978), and the line-by-line calculations reported by Chou and Arking (1980). Differences between these sets of calculations are within about 0.5°K day<sup>-1</sup>. In addition, cooling rates due to CO<sub>2</sub> emission in both standard and subarctic atmospheres have been compared with results from line-by-line computations presented by Fels and Schwarzkopf (1981). The difference near maximum cooling (~50 km) is no more than 5% (~0.4°K). The total IR cooling rate profile for a tropical atmosphere also agrees closely with that computed from a band model (Roewe and Liou, 1978) and from observations reported by Cox (1969).

In addition to the aforementioned comparisons, we perform computations of the clear-sky IR radiative cooling rate profiles for five

different model atmospheres provided by McClatchey et al. (1971), and compare them with results produced by the GFDL/NMC radiation parameterization method. The current model computations are based on the AFGL 18-layer vertical grid structure, which has been shown in Fig. 5. The AFGL 18-layer structure is identical to the NMC 18-layer structure. The AFGL 18-layer model has four layers in the stratosphere ( $\sigma < 0.2$ ) and four layers in the boundary layer region ( $\sigma > 0.875$ ). The cooling rate profiles are shown in Fig. 6a-e. In general, the IR cooling rate profiles computed from the present model agree well with the GFDL/NMC results. The differences between these two models are generally within about 0.5°K/day, except in the lower atmosphere. The largest difference is found in the tropical lower atmosphere, probably due to the treatment of water vapor continuum absorption.

#### 4.2 Adding Scheme for Radiative Transfer in Cloudy Atmospheres

A detailed narrow-band radiative transfer program was recently developed by Kinne (1987). This program employs the matrix-operator method (Rass et al., 1973), which is essentially the same as the adding method in terms of numerical computations. The solar and IR spectra are divided into a number of bands. In each band, the transmittance of atmospheric gases is approximated by a set of exponential functions.

Application of the adding principle to an inhomogeneous atmosphere is carried out by dividing the atmosphere into a number of homogeneous layers. Two steps are followed. First, the reflection R, transmission , and emission J of a layer are determined. A very thin sublayer with an optical depth  $\tau < 10^{-7}$  is used initially. For these sublayers,

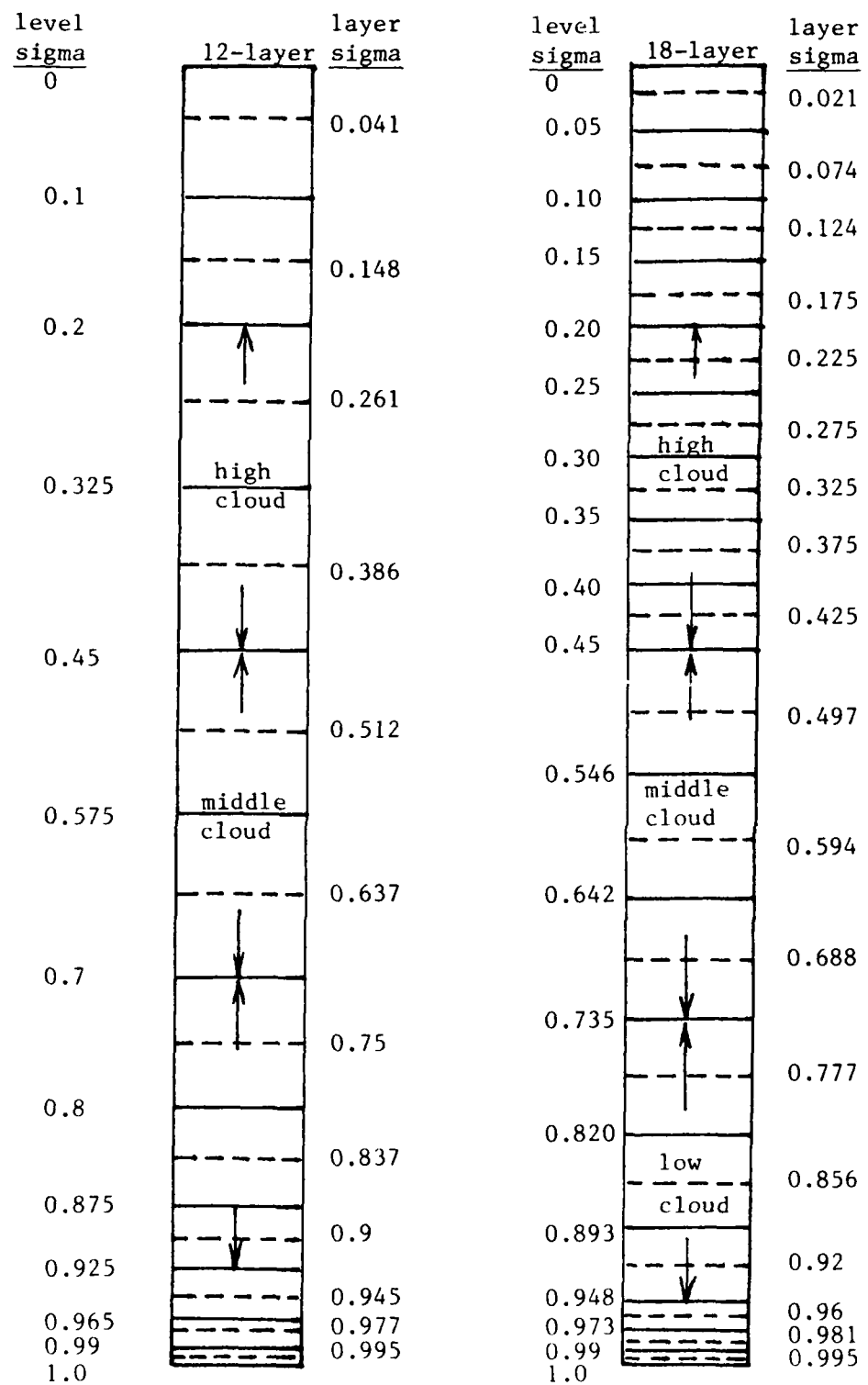


Fig. 5 Vertical grid structure used in the AFGL 12- and 18-layer models, along with specifications of high, middle, and low cloud domains.

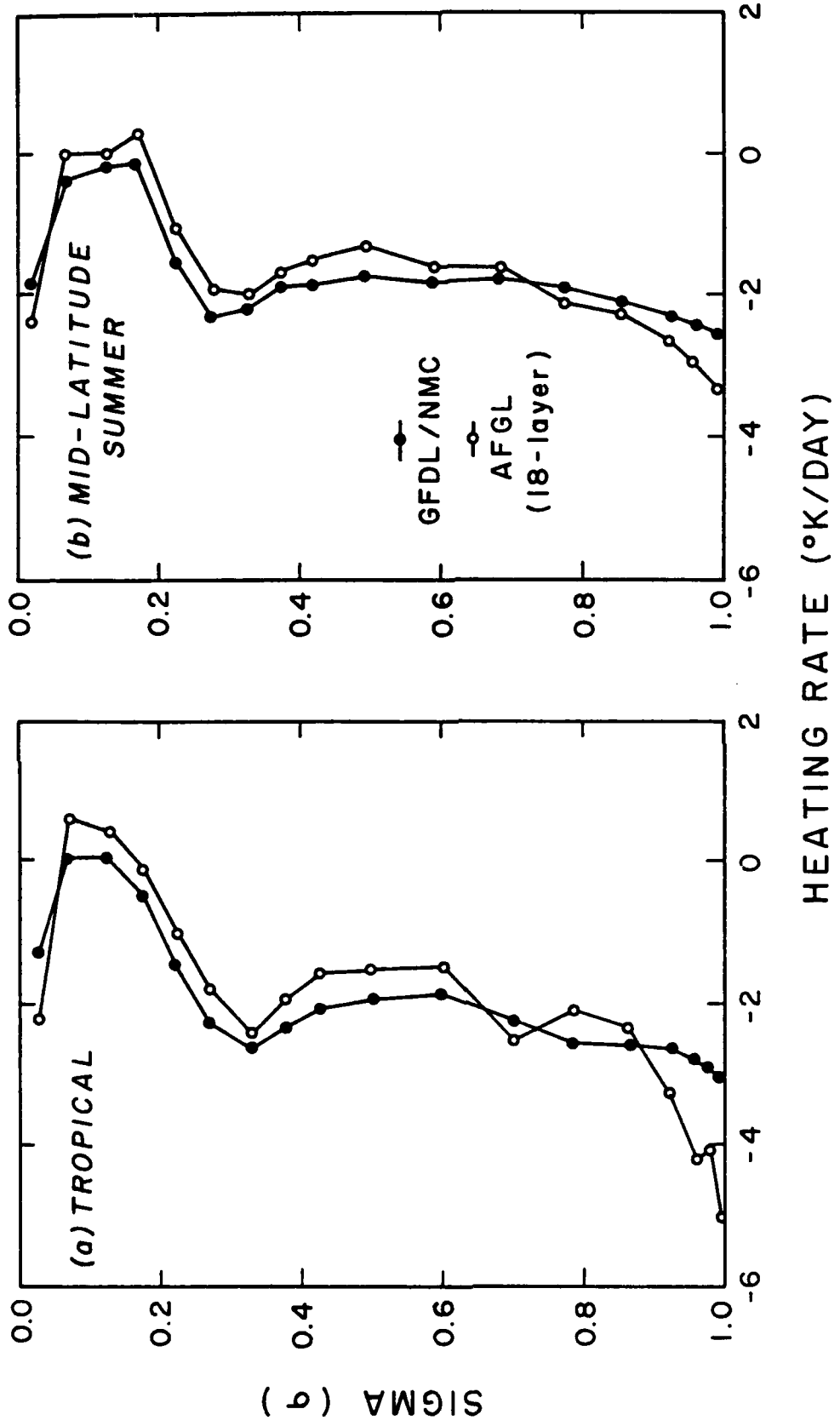


Fig. 6 Intercomparison of model-generated clear-sky IR cooling rate profiles with those from the GFDL/NMC model for (a) tropical, (b) midlatitude summer, (c) midlatitude winter, (d) subarctic summer, and (e) subarctic winter atmospheres.

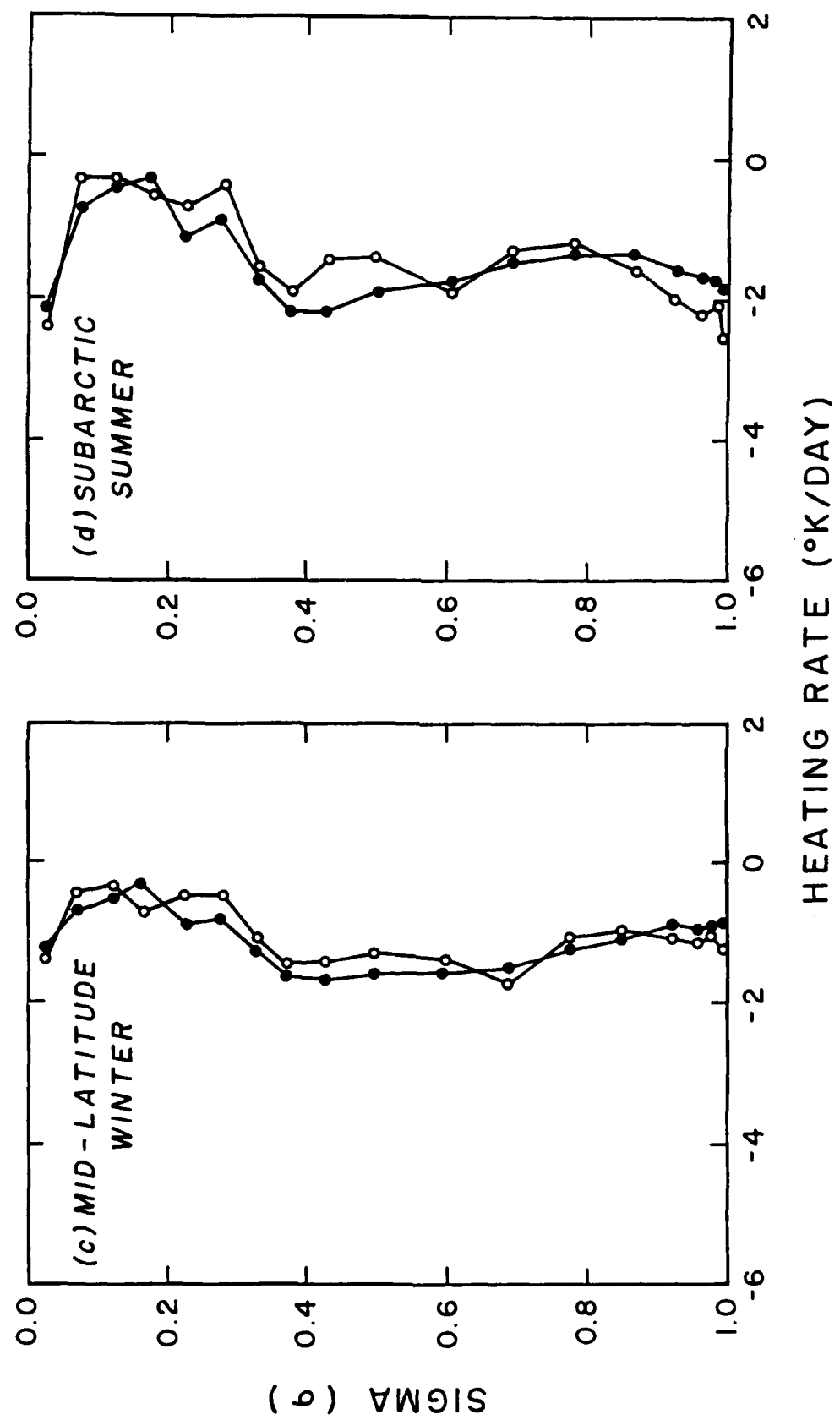


Fig. 6 (cont.)

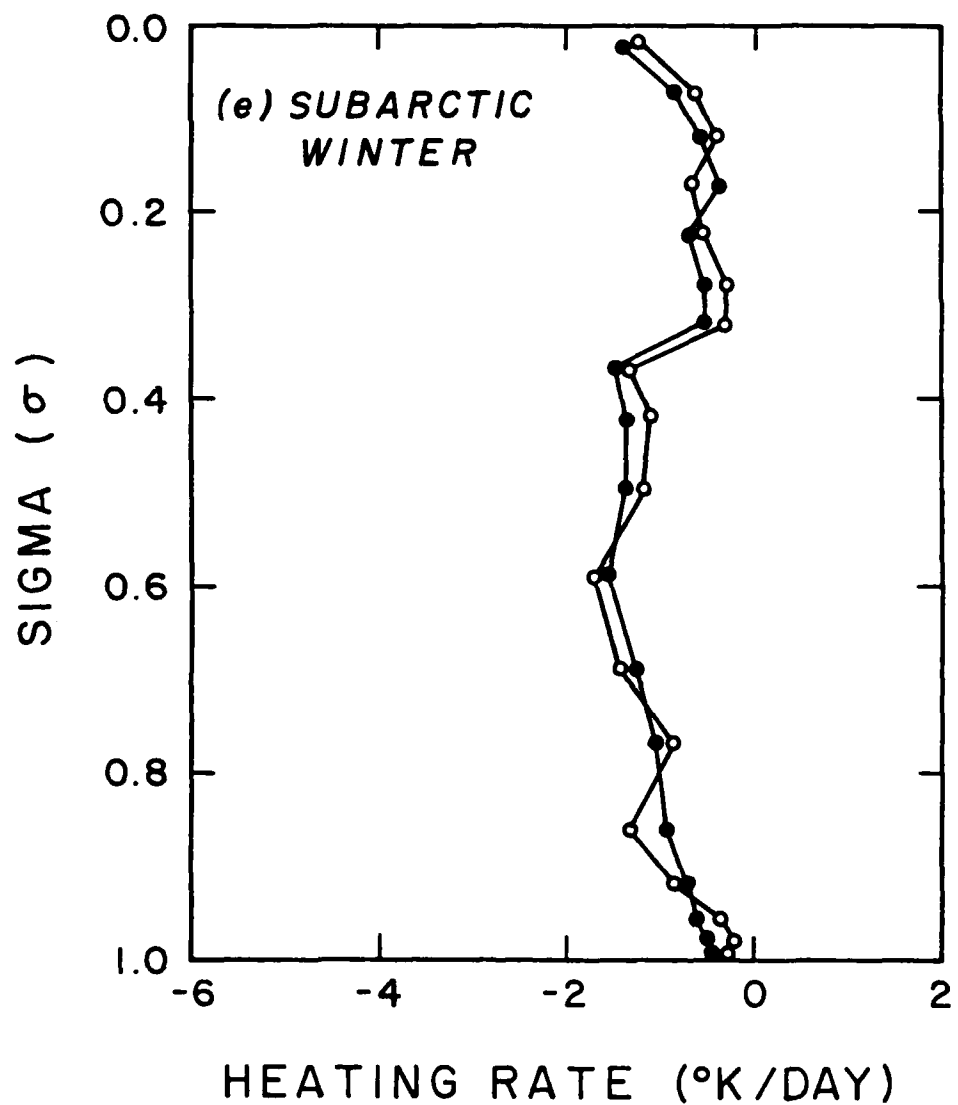


Fig. 6 (cont.)

matrices  $R$  and  $T$  and the vector  $J$  are determined in a manner such that the effects of direct solar radiation and gaseous absorption are included. Then two layers with the same optical properties are combined, until the desired optical thickness for a prescribed layer is reached. This is the doubling procedure, which is performed for all prescribed homogeneous layers.

There is now a set of  $R$ ,  $T$ , and  $J$  for all homogeneous layers. Two layers are subsequently added. Beginning from the top of the atmosphere, using the optical properties of the uppermost layer, the values of progressively lower layers are added one at a time. This adding procedure is applied for all homogeneous layers. Finally, a surface layer is added to account for the emission and reflection effects of the surface.

The resulting intensities  $I$  for various directions at each layer boundary are summed to obtain the hemispheric fluxes  $F^+$  and  $F^-$ . From the divergence of the net flux  $F^N$  at the boundaries of a given layer, the layer heating and cooling rates are determined. The cooling rate results to be shown in this section were obtained based on a spectral resolution of 8 solar and 12 IR bands approximated by exponential functions of a total of 120 terms, and on five equal intervals of the zenith angle. The inhomogeneous atmosphere is divided into 18 layers.

With the exception of the ozone data at solar wavelengths, which are taken from measurements by Vigroux (1953), all data for gaseous absorption are based on spectral transmittance data computed from line-by-line data compiled by McClatchey et al. (1971) and updated by Rothman et al. (1983). For water clouds, the spectral distribution of refractive indices is taken from values provided by Downing and Williams (1975), and

the single-scattering albedo and asymmetry factor were computed using Mie scattering theory. For ice clouds, the refractive indices for ice were taken from values tabulated by Schaaf and Williams (1973). The single-scattering albedo and asymmetry factor were approximated by those of spherical water droplets with the same surface area, but with adjustments to account for the hexagonal structure of ice particles. The particle size distributions used for single-scattering calculations for high, middle, and low clouds follow, respectively, those for cumulus, altostratus, and cirrostratus (Liou and Wittman, 1979).

#### 4.3 Intercomparison of Cloudy-Sky Radiative Heating Rates

Utilizing the new scheme for computing the radiative heating rate in cloudy atmospheres as described in Section 3, we carry out intercomparisons between results from the present model and those from the doubling/adding scheme. The present computation is based on the AFGL 18-layer vertical grid structure, as shown in Fig. 5. Figure 5 also shows the vertical domain for each of the three cloud decks. Clouds are assumed to fill respective vertical domains. The atmospheric profile used for flux calculations is the 1962 U.S. Standard Atmosphere. Computations were made for seven cloud configurations including three one-deck, three two-deck, and one three-deck clouds. In the infrared region, the high cloud radiative properties were prescribed based on a liquid water content of  $0.006 \text{ g/m}^3$ . In the solar region, the cloud radiative properties were calculated using the parameterizations of Liou and Wittman (1979). The cosine of the solar zenith angle is chosen to be 0.8 and the surface albedo is 0.2.

Figure 7a-h shows the results of IR radiation intercomparisons. The plots include IR radiative cooling rates obtained from the current parameterization method, as well as from the doubling/adding model using the AFGL 18-layer structure. In general, the cooling rate profiles agree with each other rather well in the clear atmosphere case with deviations less than  $0.3^{\circ}\text{C/day}$  (Fig. 7a). They are also quite close to each other for clear regions separated by clouds as shown in Fig. 7b-h. Larger differences are noted between intracloud cooling rate values. For high clouds, agreement between the current parameterization and the doubling/adding scheme is better near the cloud top and base than in mid-cloud regions, where differences are on the order of  $\sim 1^{\circ}\text{K/day}$ . The present parameterization reproduces quite realistically cloud top cooling and base warming. This appears to demonstrate the validity of the exponential interpolation for computations of intracloud fluxes. For middle and low clouds, excellent agreement is shown between the two sets of results, suggesting the propriety of the blackbody assumption. The cloud top cooling for middle and low clouds is on the order of  $-10$  and  $-12^{\circ}\text{K/day}$ , respectively. In the cases with two-deck clouds, cooling is reduced due to downward emission by the higher cloud base. The cloud base heating for middle and low clouds is on the order of  $3.5$  and  $1.7^{\circ}\text{K/day}$ , respectively. In mid-cloud regions, there is no heating as a result of constant net fluxes, which are close to zero. Zero net flux indicates that the upward and downward fluxes at that level are equal. In the case where both middle and low clouds are present (Fig. 7g,h), cooling near the boundary of these two clouds is also zero, since the two cloud decks are contiguous.

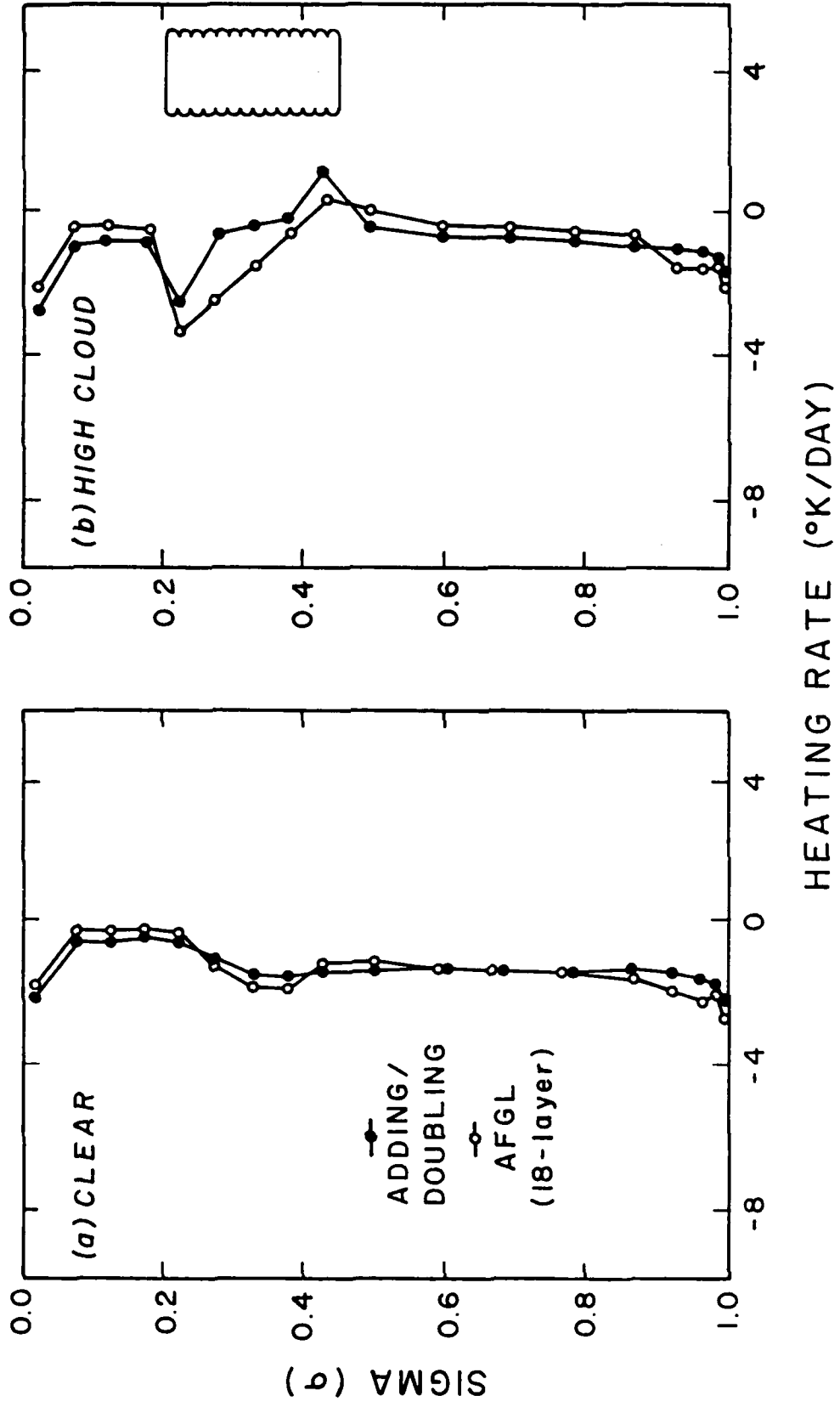
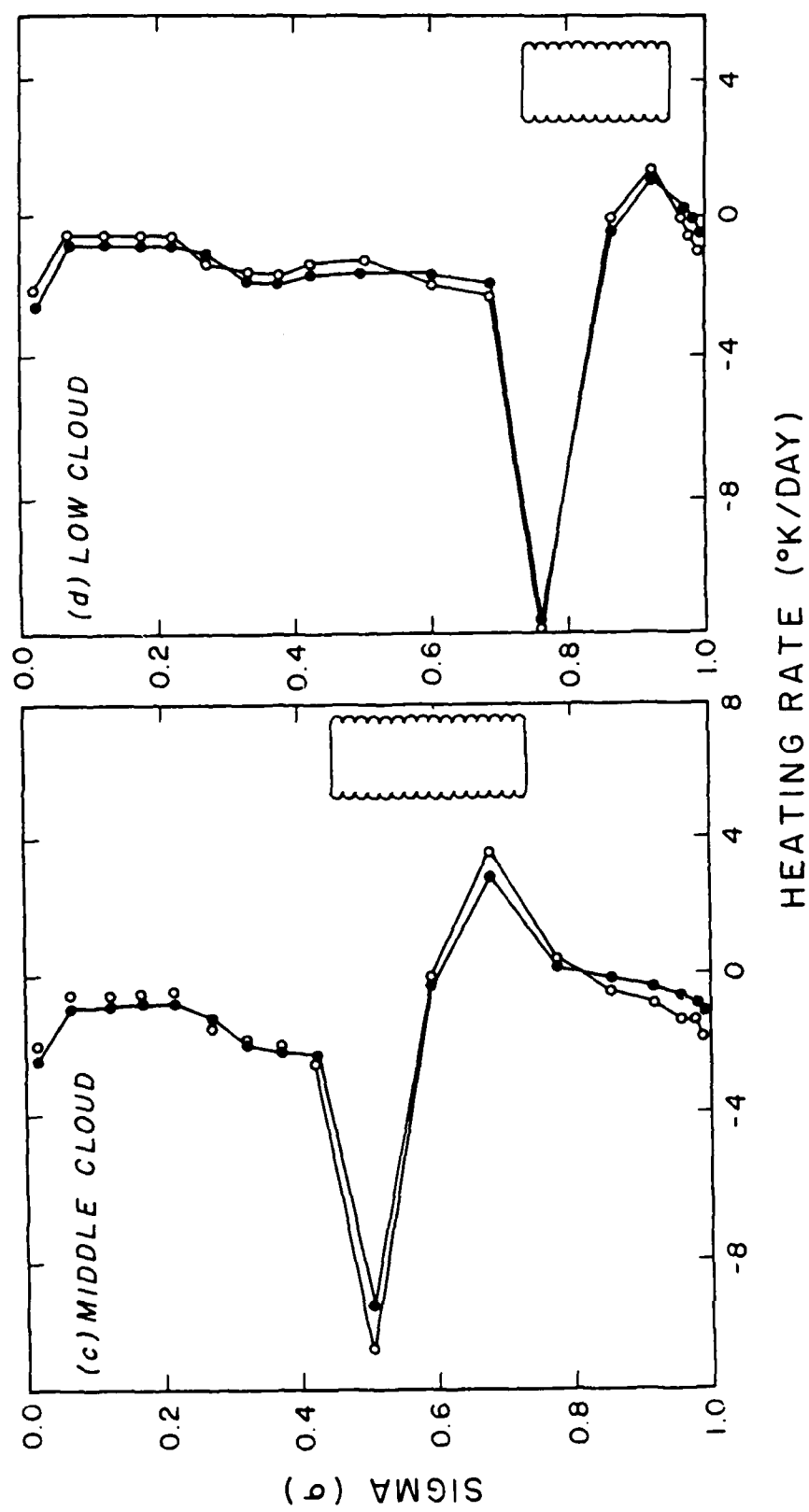


Fig. 7 Intercomparison of model-generated IR cooling rate profiles with those from the doubling/adding scheme based on the 1962 U.S. Standard Atmosphere for different cases: (a) clear, (b) high cloud only, (c) middle cloud only, (d) low cloud only, (e) high and middle clouds, (f) high and low clouds, (g) middle and low clouds, and (h) high, middle, and low clouds.

FIG. 7 (cont.)



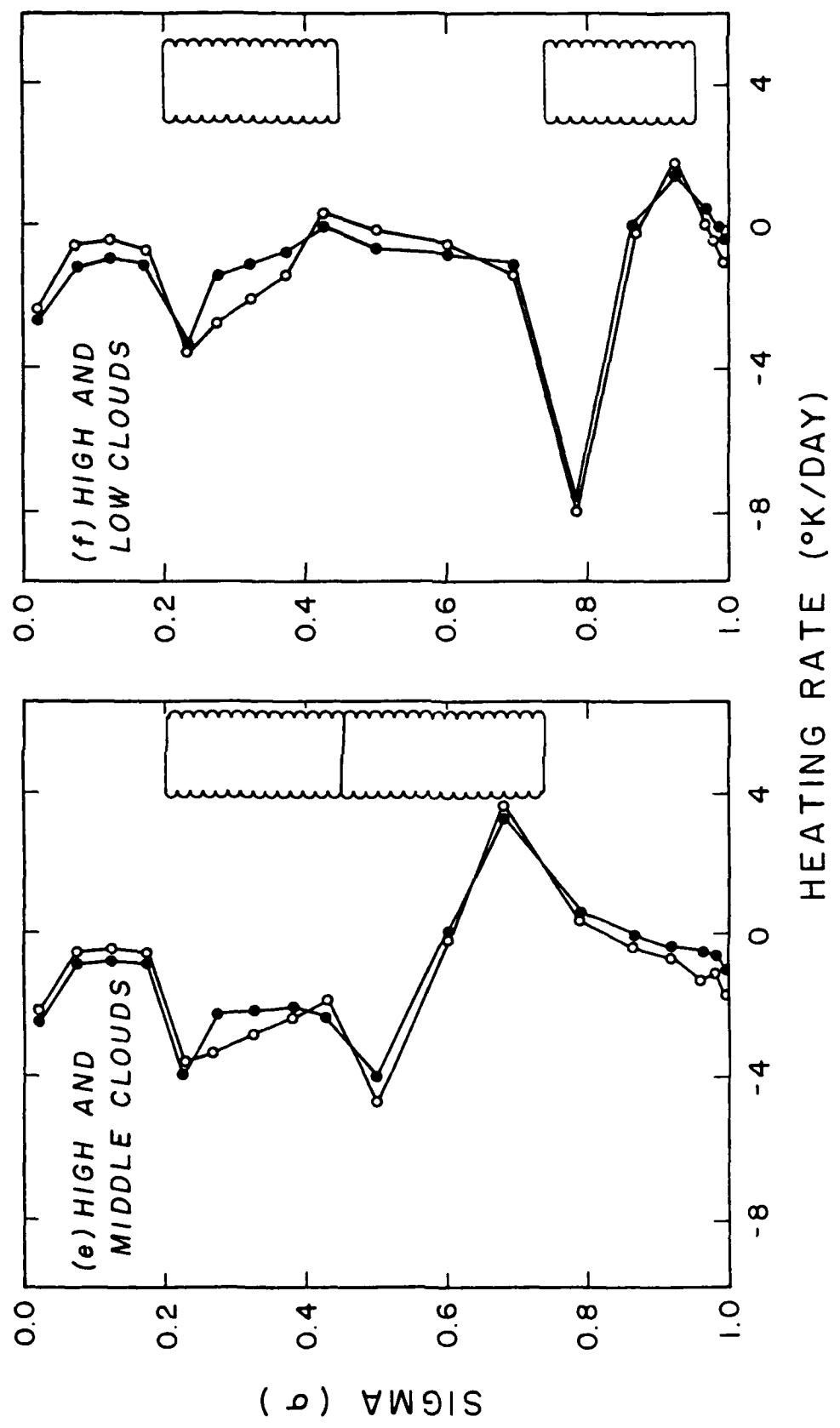


Fig. 7 (cont.)

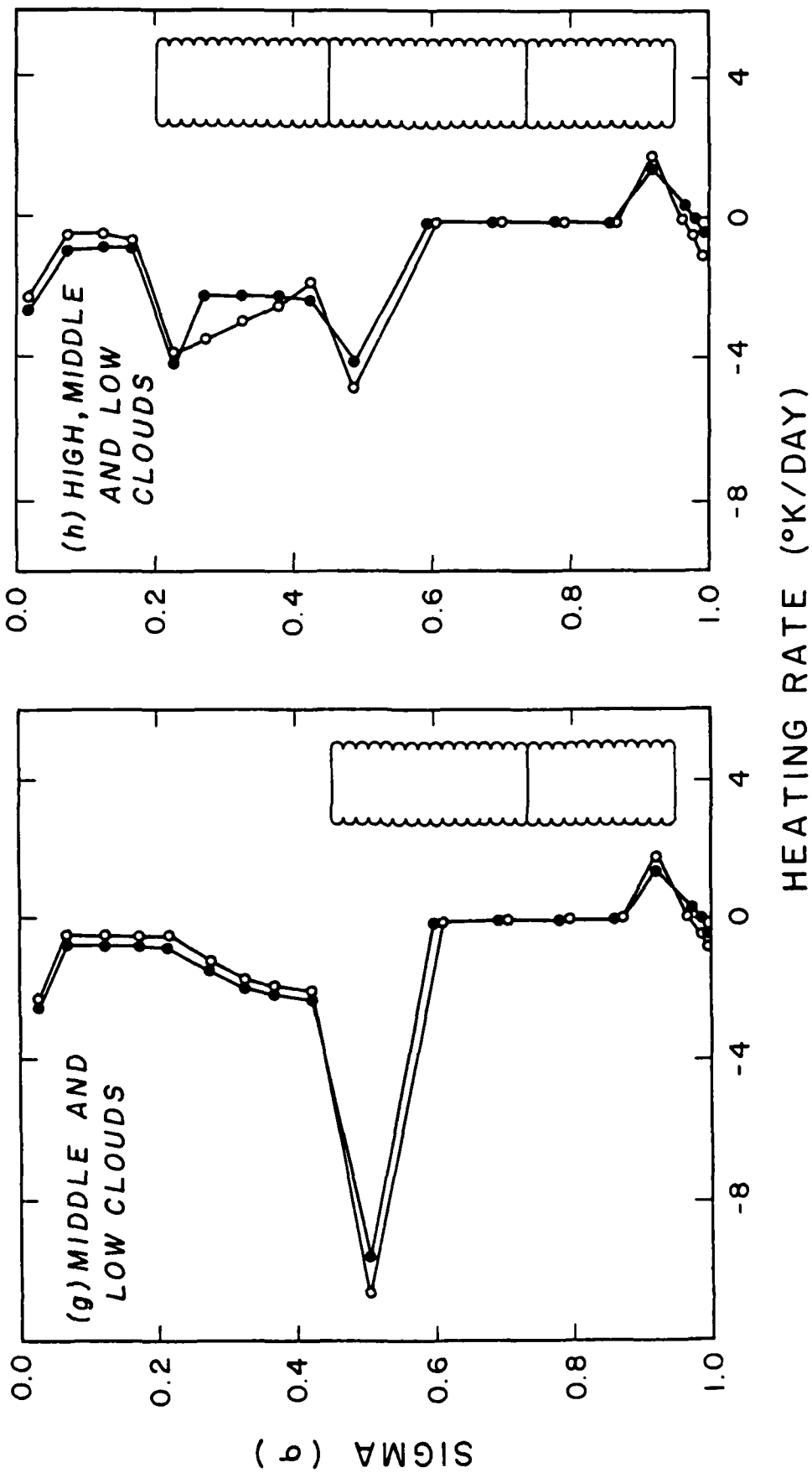


Fig. 7 (cont.)

Figure 8a-h shows the results of solar radiation intercomparisons. In general, heating rate profiles for the clear atmosphere agree well with each other in the troposphere, with differences of no more than  $0.5^{\circ}\text{K/day}$ . In the stratosphere, the present parameterization produces slightly larger heating rates than the doubling/adding scheme. Good agreements are also evident for heating rate profiles in clear regions separated by clouds, as shown in Fig. 8b-h. Within each cloud deck, larger differences are shown. These differences may be caused by the use of broadband cloud radiative properties in the parameterization. In general, the present parameterization correctly produces the pattern of cloud top heating. For high clouds, the parameterization produces less heating than the doubling/adding scheme, but the difference is no more than  $1^{\circ}\text{K/day}$ . For middle and low clouds, the difference between the current parameterization and the doubling/adding scheme is within  $2^{\circ}\text{K/day}$ . In the case of one-deck clouds (Fig. 8b-d), heating peaks of about 8 and  $9.5^{\circ}\text{K/day}$  at the cloud top are generated by middle and low clouds, respectively. In the case of two-deck clouds (Fig. 8e-g), if the upper deck is the high cloud, the heating rate profiles for middle or low clouds do not change significantly. However, for a combination of middle and low clouds, heating rates below the optically thick middle cloud become very small. This is also evident for the three-deck cloud case. In summary, the present broadband parameterization programs for the transfer of IR and solar fluxes produce reliable heating/cooling profiles in various cloudy conditions. The maximum deviation of about  $2^{\circ}\text{K/day}$  occurs for the solar heating rate at the low cloud top. Other deviations produced by this efficient and economic parameterization scheme are all within about  $1^{\circ}\text{K/day}$ .

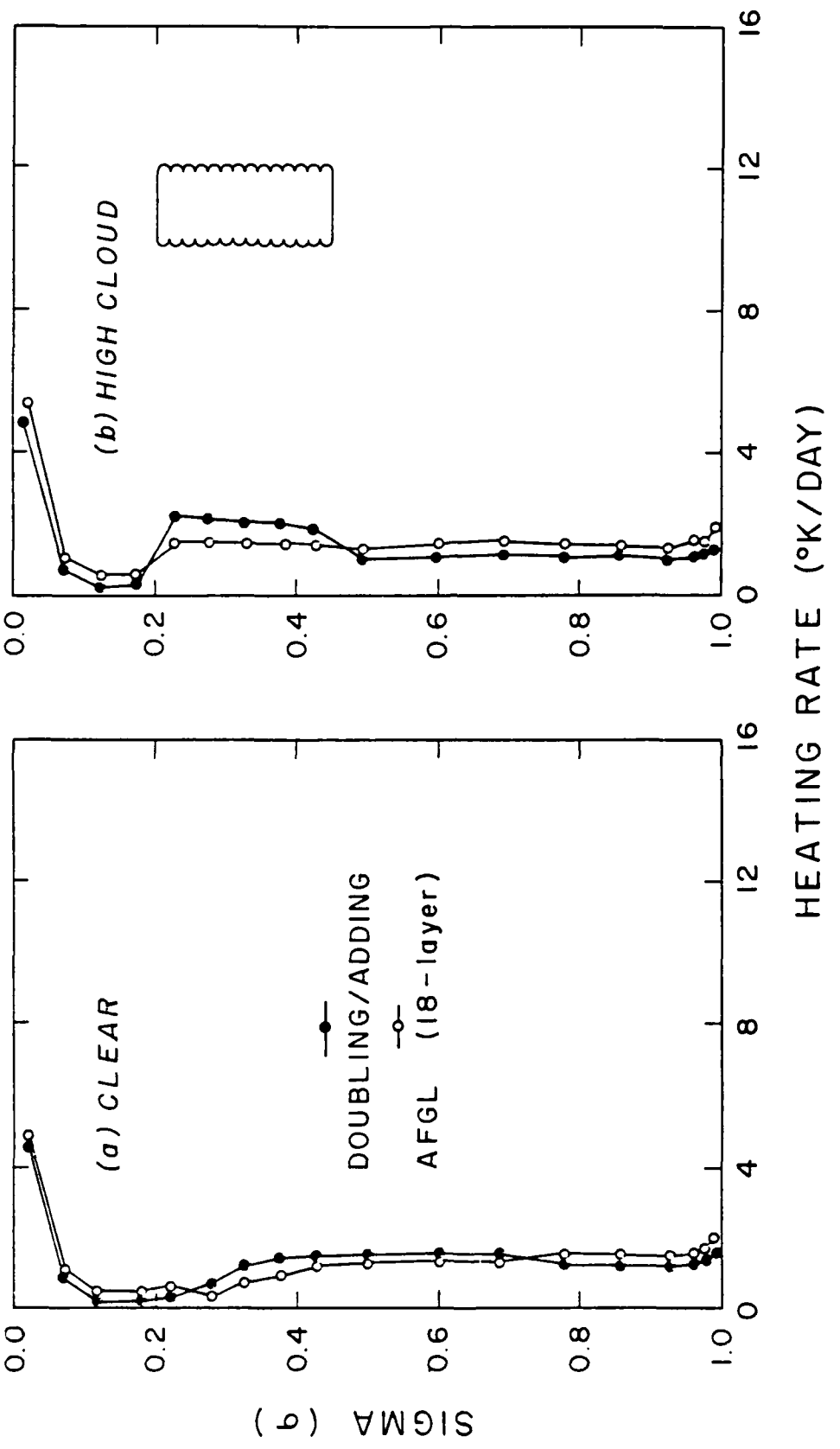
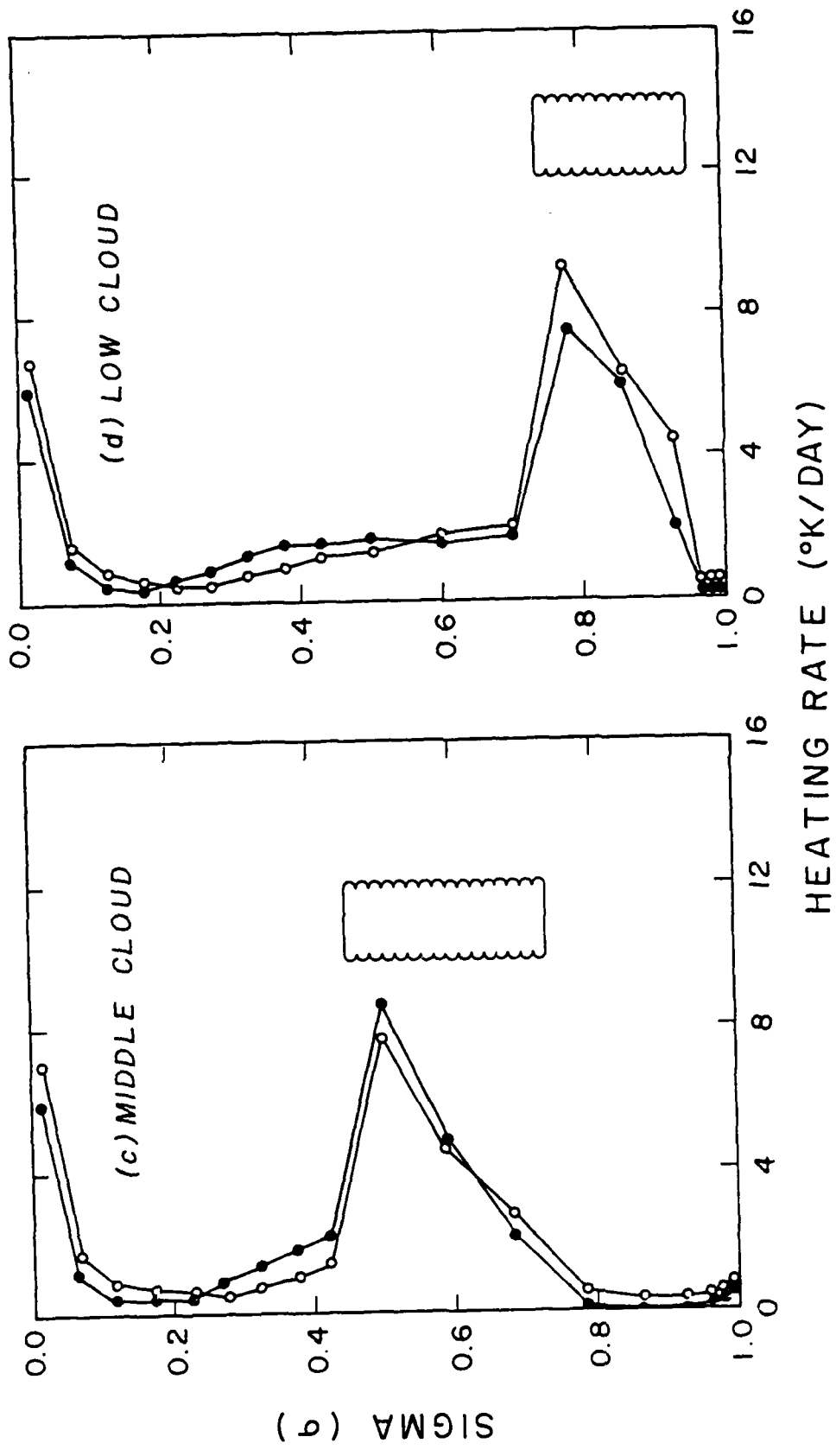


Fig. 8 Intercomparison of model-generated solar heating rate profiles with those from the doubling/adding scheme based on the 1962 U.S. Standard Atmosphere for different cases: (a) clear, (b) high cloud only, (c) middle cloud only, (d) low cloud only, (e) high and middle clouds, (f) high and low clouds, (g) middle and low clouds, and (h) high, middle, and low clouds.

FIG. 8 (cont.)



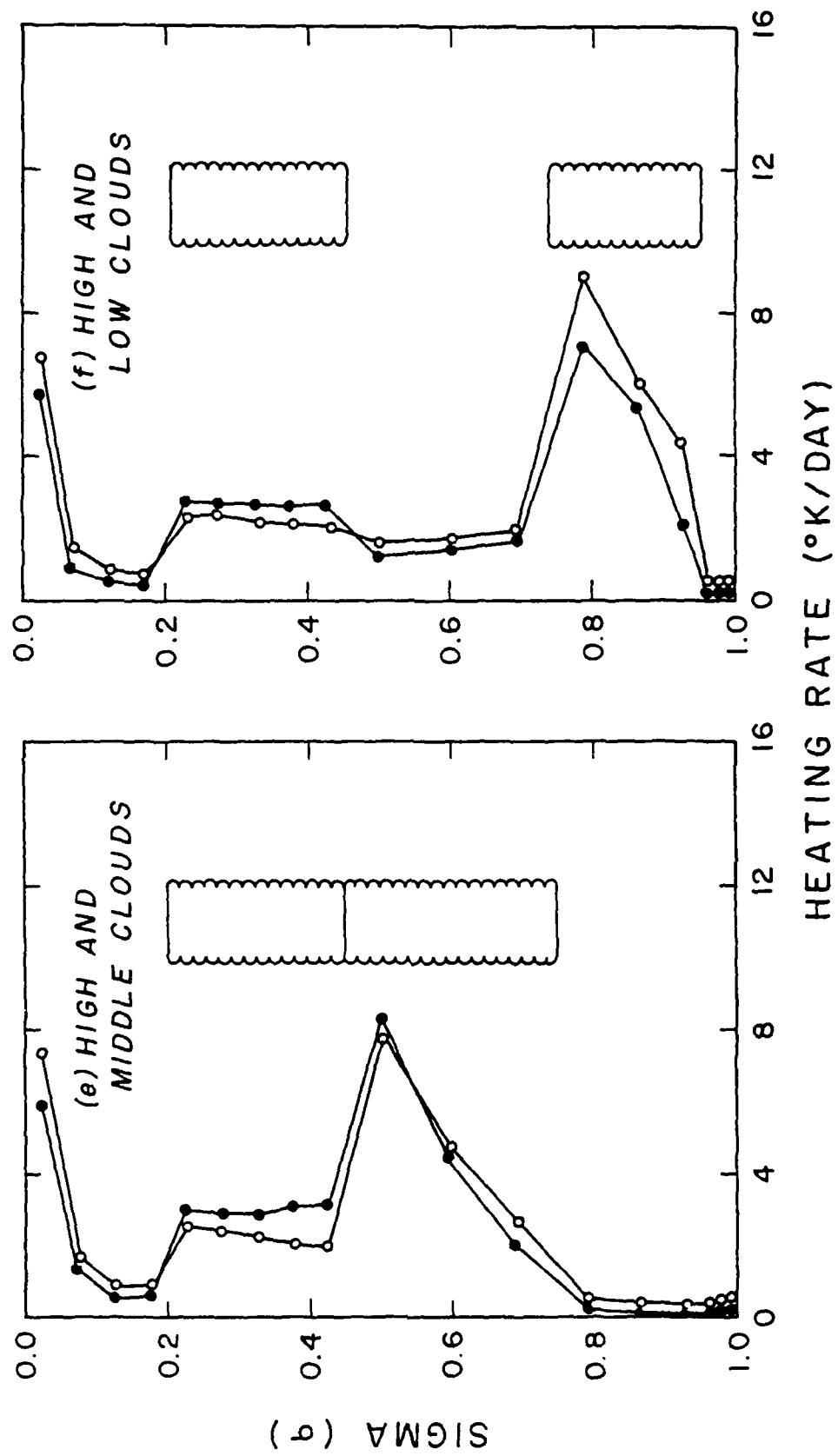


Fig. 8 (cont.)

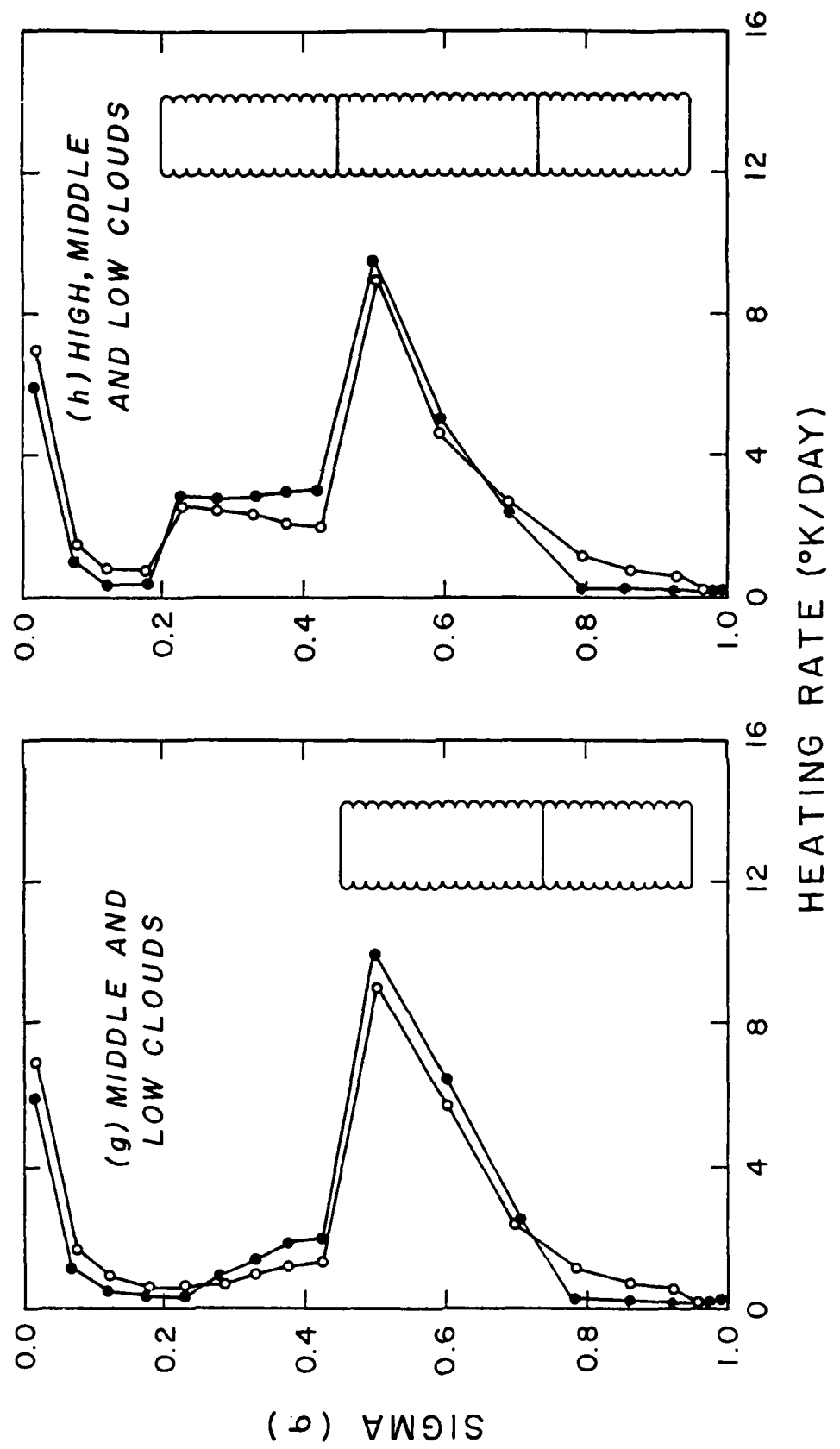


Fig. 8 (cont.)

## Section 5

### RESULTS OF CLOUD AND RADIATION BUDGET FIELDS

#### 5.1 Cloud Prediction

Using the AFGL 12-layer GCM and the initial field of 12Z, 17 June 1979, which consists of temperature and specific humidity data, clouds are formed according to the method described in subsection 3.1.1. The multiple-layer cloud field is then strapped into at most three decks of clouds using the scheme described in subsection 3.1.2. Subsequently, the total cloud cover field is generated using the maximum overlap assumption. The zonally-averaged latitudinal distribution of high, middle, low, and total cloud cover for one time step is shown in Fig. 9a-d. The high cloud cover is mostly ~10%, except near the South Pole, where it reaches more than 40%. The middle cloud cover reaches 40% near 10°N and 80% near 80°S, but decreases to less than 10% in the subtropics. The low cloud distribution is similar to that for middle clouds except near the North Pole region, where more low clouds are present. The total cloud cover distribution is slightly lower than the summer cloud climatology of London (1957).

#### 5.2 Radiation Budget

The global distributions of outgoing IR and net downward solar fluxes at the top of the atmosphere (TOA) and surface are computed from the AFGL 12-layer GCM. The zonally averaged latitudinal distributions of these quantities are shown in Fig. 10a-d. The outgoing IR flux at the

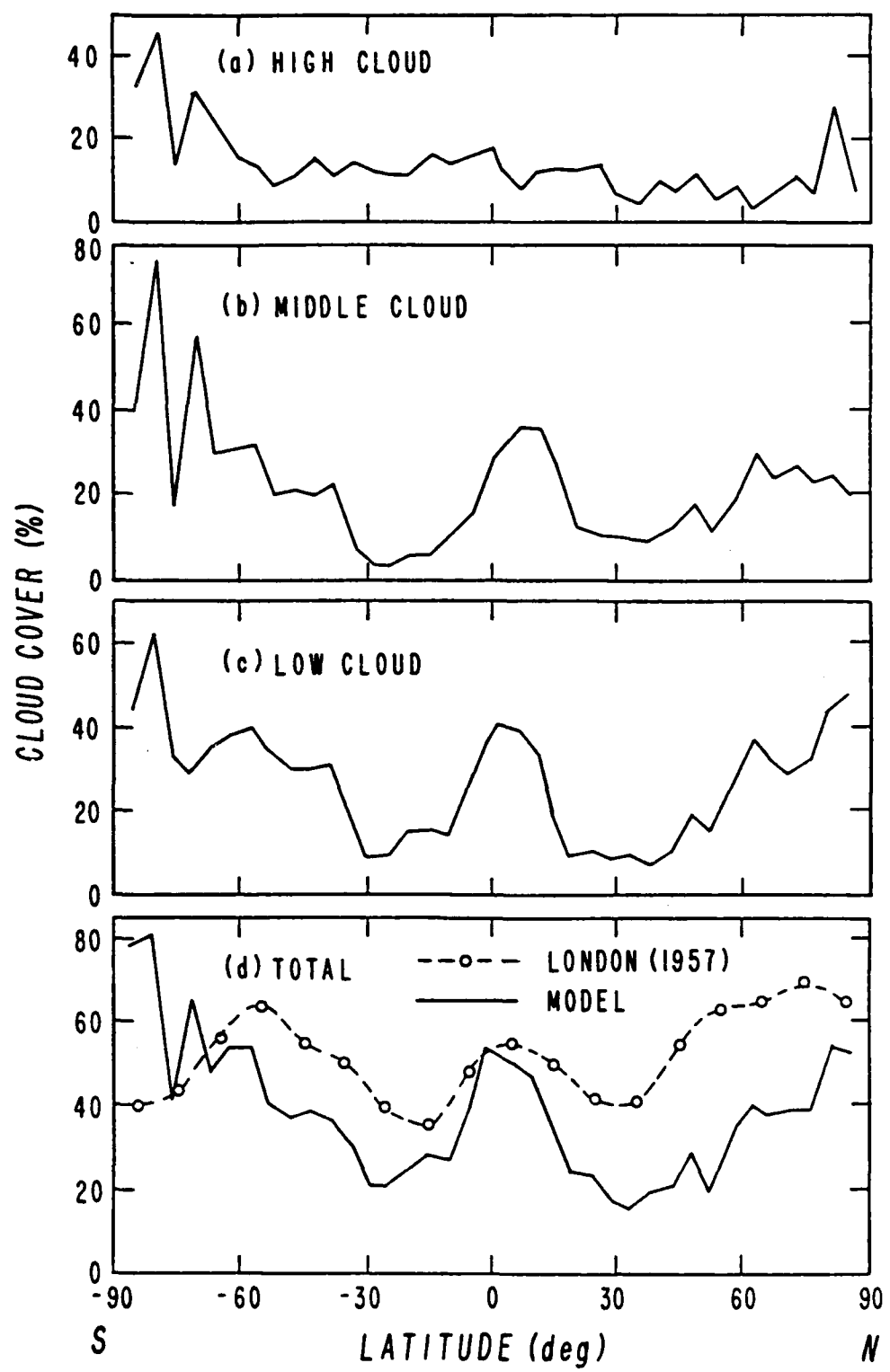


Fig. 9 Zonally averaged latitudinal cloud cover distribution based on the initial temperature and humidity field of 12Z, 17 June 1979.  
 (a) high cloud, (b) middle cloud, (c) low cloud, and (d) total.

TOA (Fig. 10a) is lowest near the South Pole ( $\sim 110 \text{ W/m}^2$ ), and increases northward to about  $260 \text{ W/m}^2$  in the southern subtropics. It decreases to  $240 \text{ W/m}^2$  and increases to  $270 \text{ W/m}^2$  near  $30^\circ\text{N}$ . An IR flux of  $200 \text{ W/m}^2$  is found near the North Pole. Low values in the Southern Hemisphere are caused by the low temperatures of the southern winter. The minimum in the tropics is due to the combined effects of high humidity and cloudiness. The net solar flux at the TOA (Fig. 10b) is 0 near the South Pole, increases to  $280 \text{ W/m}^2$  near  $5^\circ\text{S}$  before a slight decrease to  $230 \text{ W/m}^2$ . It increases to a maximum of  $\sim 400 \text{ W/m}^2$  near  $35^\circ\text{N}$  and drops to  $230 \text{ W/m}^2$  near the North Pole. The maximum in the northern subtropics is due to the combined effects of high solar zenith angles in the polar region and large fractional sunlit areas in this latitudinal belt. The peak value ( $\sim 400 \text{ W/m}^2$ ) is larger than the satellite-derived maximum ( $\sim 340 \text{ W/m}^2$ ) for the summer season (Stephens et al., 1981). This is expected since the present calculation is for 17 June, which is only five days away from the summer solstice. The distribution of surface net IR fluxes (Fig. 10c) shows that the average surface IR flux varies between  $20$  and  $90 \text{ W/m}^2$ . A large dip is present in the equatorial area, due to the combined effect of clouds and humidity. Finally, the pattern of net downward solar fluxes at the surface is similar to that of net solar fluxes at the TOA, except the values are smaller by about  $0\text{--}100 \text{ W/m}^2$ . This difference is attributed to atmospheric absorption, which depends on the solar zenith angle and humidity distribution. The highest absorption occurs near the equatorial region due to higher humidity.

### 5.3 Radiative Cooling Rates in the Atmosphere

Net radiative heating rates were calculated using the current

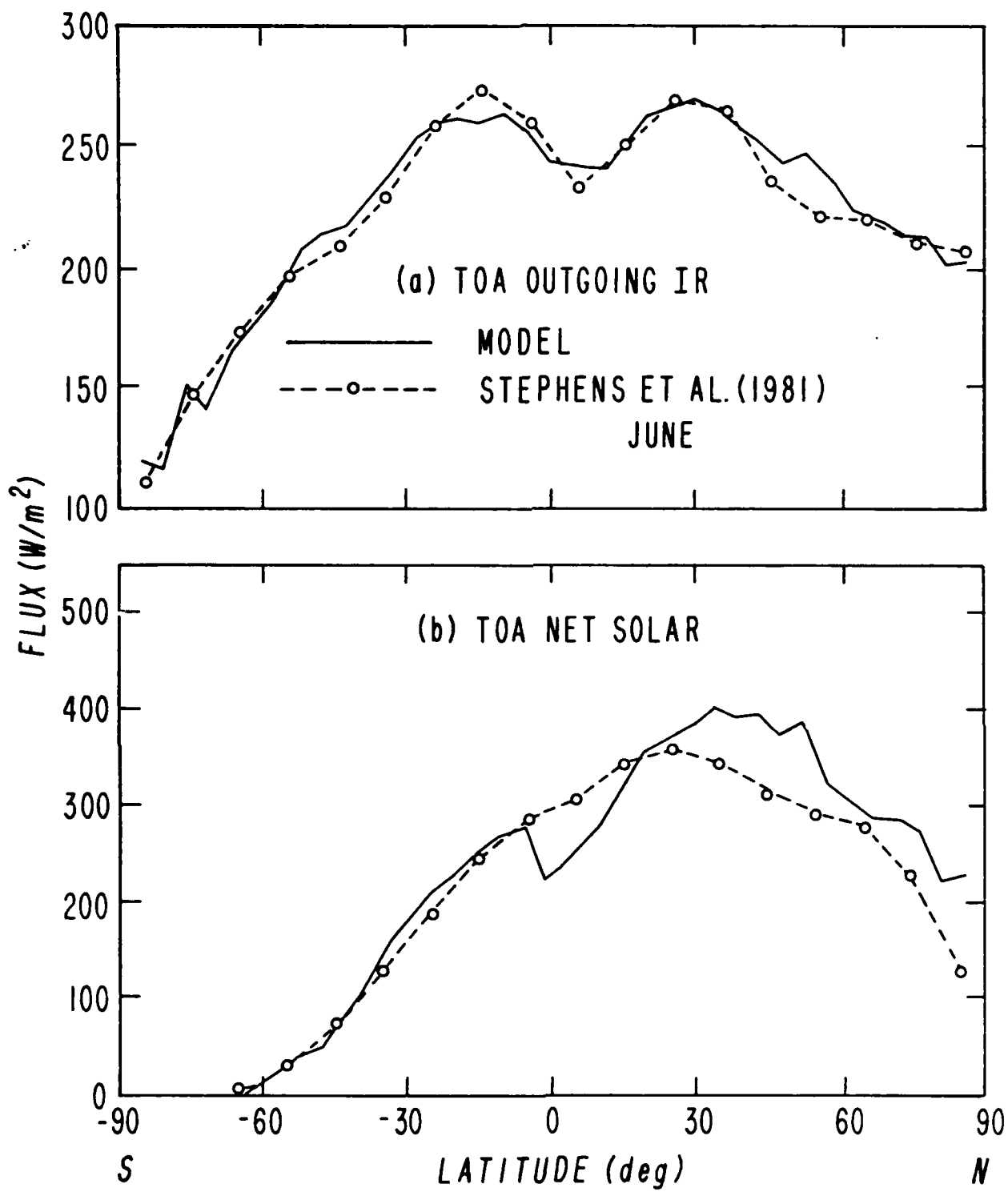


Fig. 1. Comparisons between the (solid) model and the (dashed) data of Stephens et al. on the initial temperature and humidity field of 12Z, 17 June 1979. (a) Top-of-the-atmosphere (TOA) outgoing IR flux, (b) TOA net solar flux, (c) surface net IR flux, and (d) surface net solar flux.

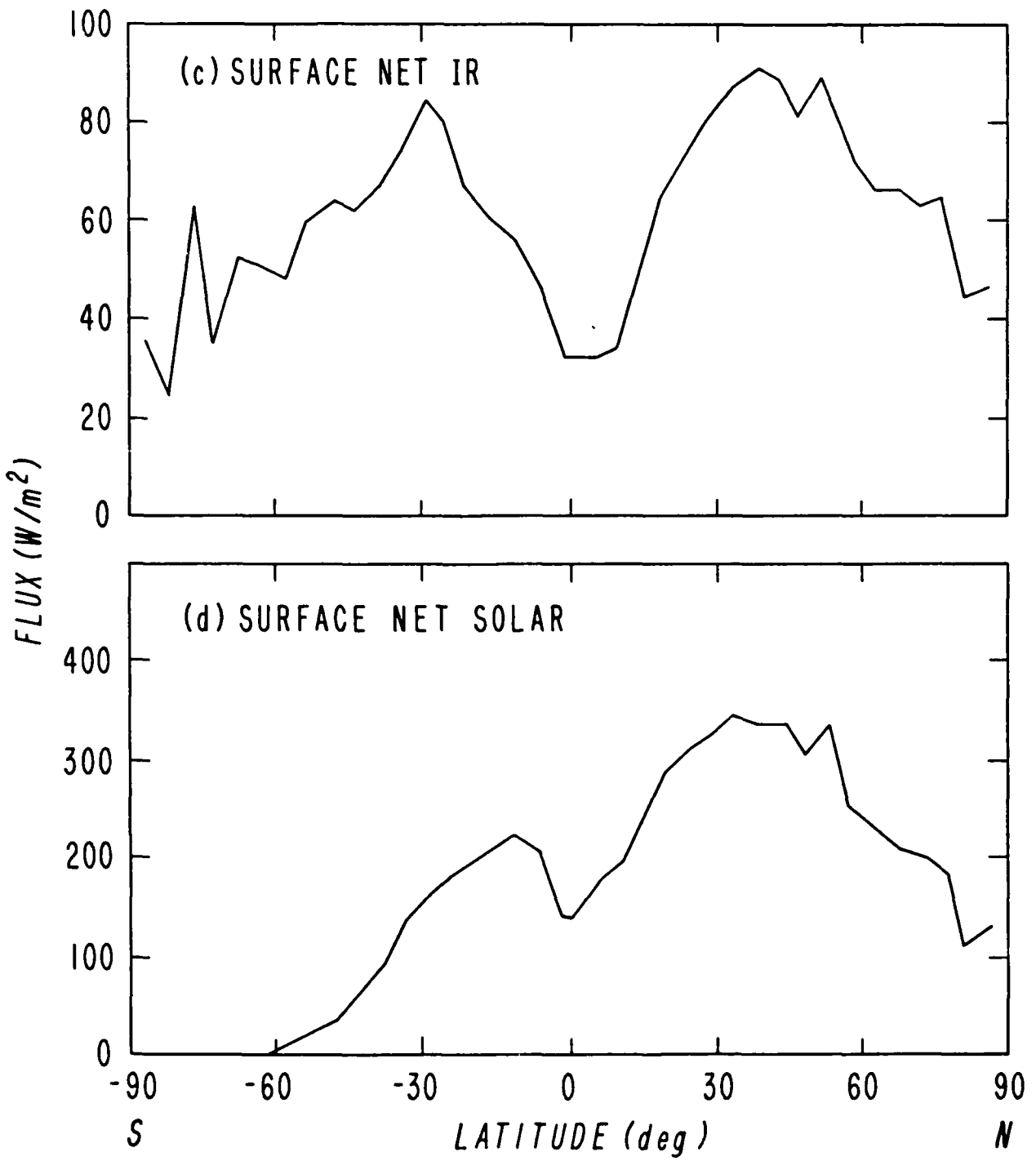


FIG. 10. (cont.)

radiation and cloud model with a 12-layer structure. The zonally averaged latitude-sigma distributions of the net radiative heating rate for clear and model-generated cloudy atmospheres, as well as the difference between the two are presented in Fig. 11a-c. For the clear case (Fig. 11a), the net cooling in the troposphere increases from the tropopause toward the surface. It ranges between 0 and  $-4^{\circ}\text{K/day}$ . The large cooling near the surface layers in the equatorial region is due to the contribution of water vapor continuum absorption. Somewhat larger cooling is present near the South Pole due to the lack of solar insolation in the antarctic. Near the North Pole, however, there is a slight warming due to absorption of solar radiation in the long arctic day. The northern stratosphere also shows a slight warming due to ozone absorption.

Compared with the clear case, the net cooling produced by cloudy atmospheres is smaller in the tropical troposphere and the lower troposphere of the Southern Hemisphere. The effect of clouds on the net cooling can be seen in Fig. 11c, where the latitude-sigma distribution of net cooling differences is shown. Below  $\sigma = 0.84$ , clouds have a warming effect. Between  $\sigma = 0.64$  and  $0.84$ , several areas of cooling are present, but cooling is not present between the equator and  $60^{\circ}\text{N}$ , presumably due to absorption of strong solar solar insolation by clouds. Above  $\sigma = 0.51$ , clouds generate cooling everywhere in the upper troposphere. Since the model middle and high cloud tops are located at  $\sigma = 0.45$  and  $0.2$ , respectively (Fig. 5), the net cooling there is directly associated with strong cloud top cooling. In addition, the IR emission of high clouds outweighs the absorption due to solar radiation. As a result, the presence of high clouds produces cooling at the cloud top.

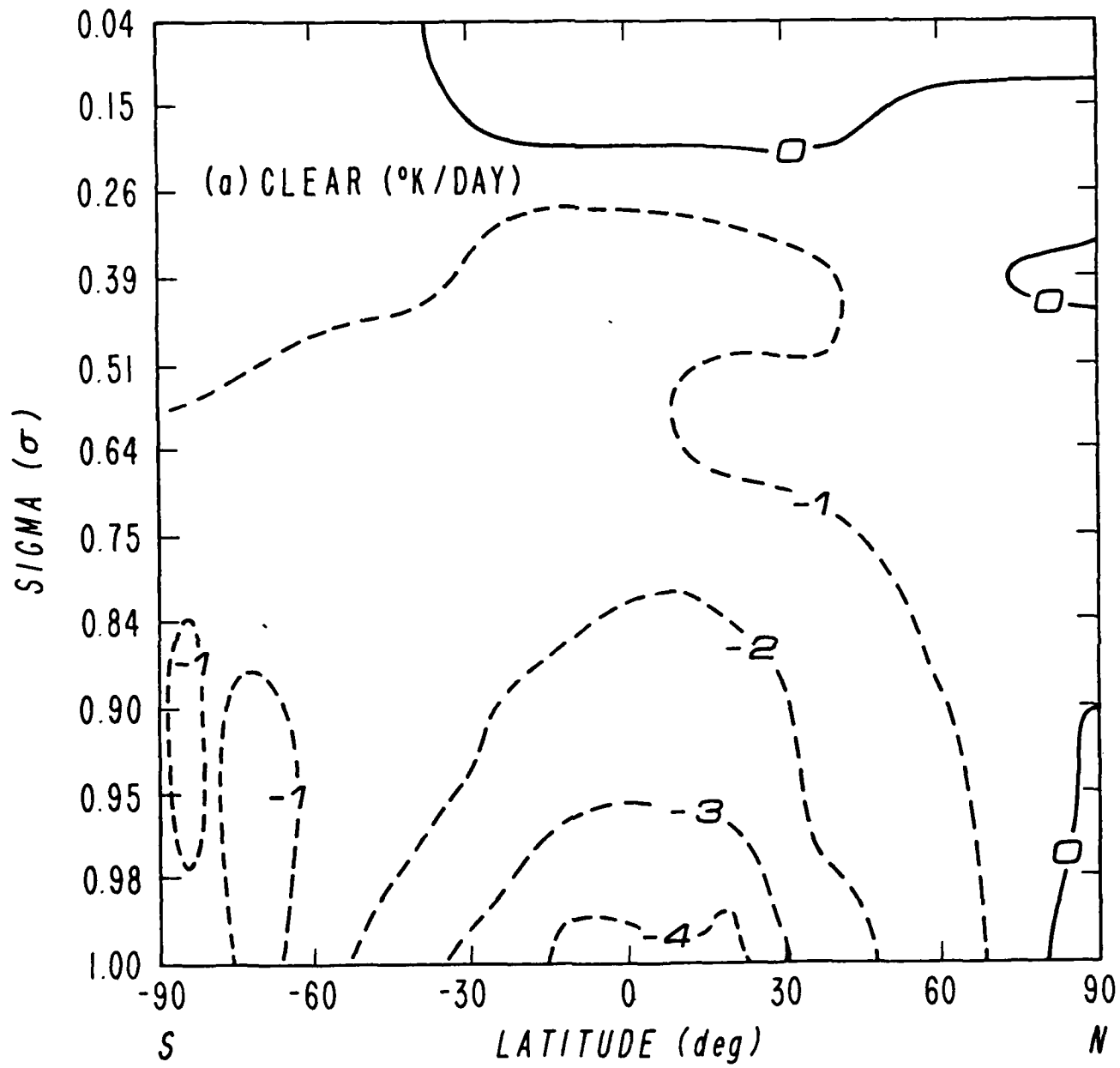


Fig. 11 Zonally averaged latitude-height ( $\sigma$ ) distribution of net (IR-solar) radiative heating rate based on the initial field of 12Z, 17 June 1979. (a) Clear sky, (b) cloudy sky, and (c) difference between cloudy and clear heating rates. Units:  $^{\circ}\text{K}/\text{day}$ .

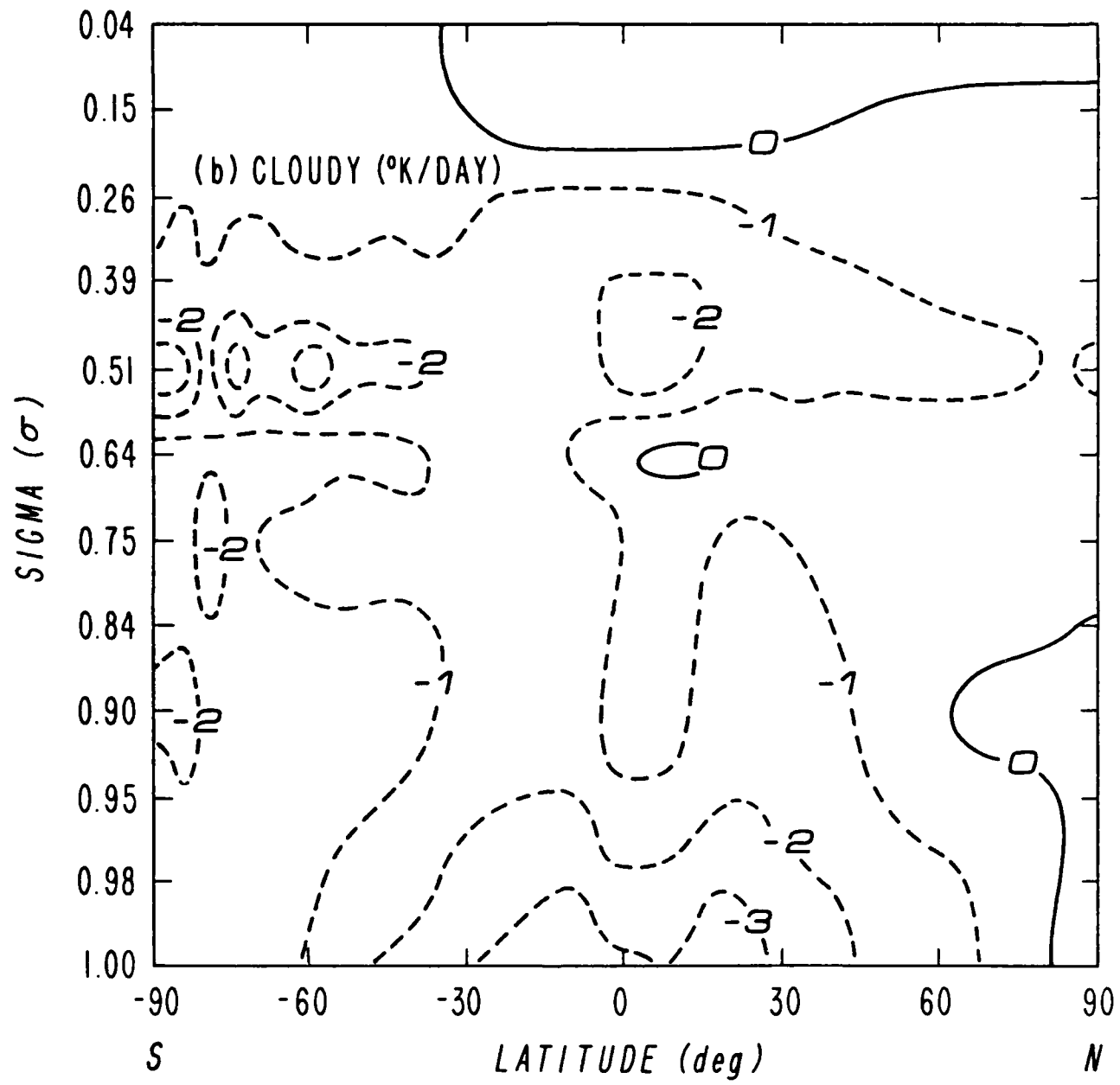


Fig. 11 (cont.)

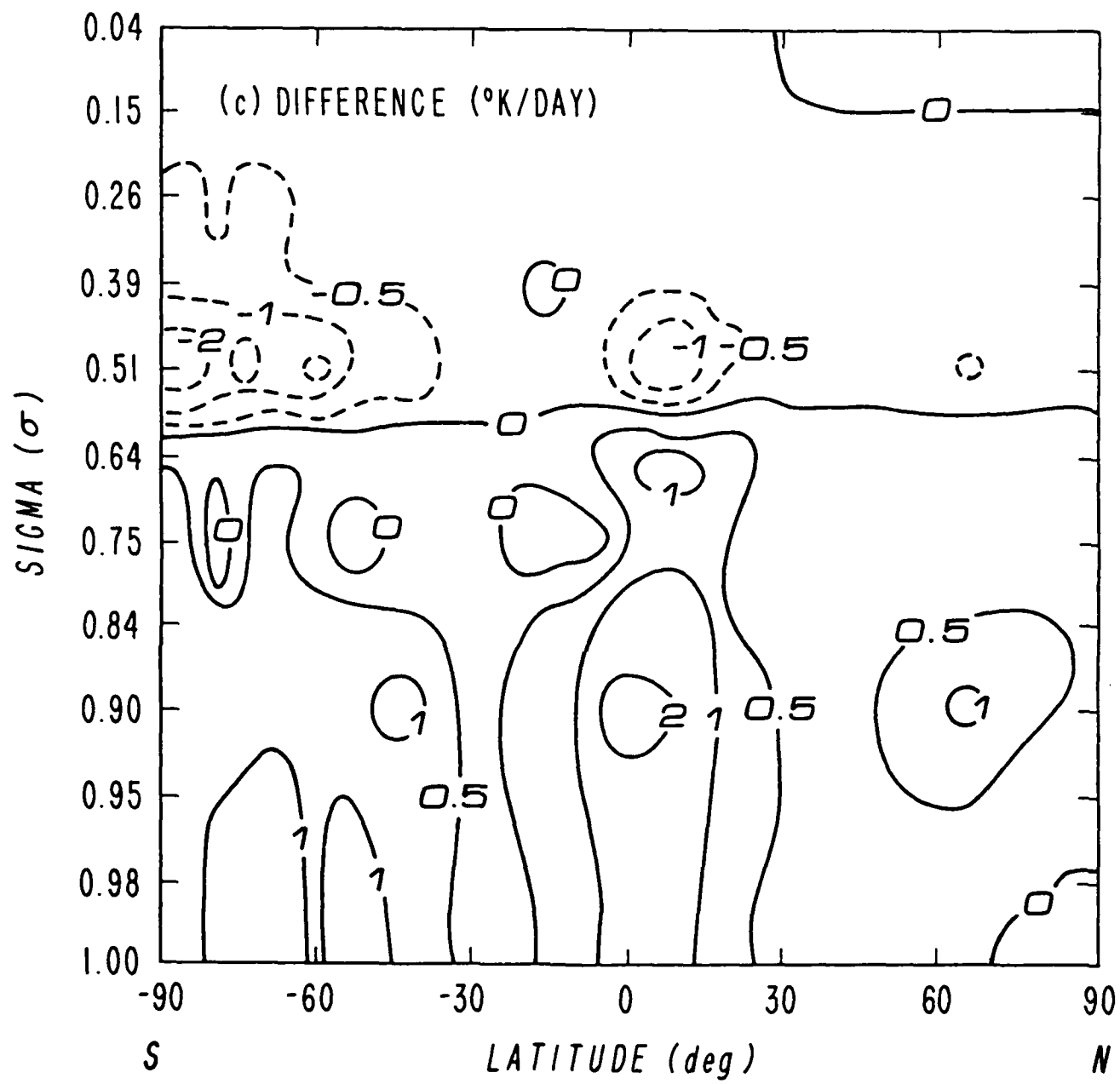


Fig. 11 (cont.)

## Section 6

### SUMMARY

In this report, we have described the IR and solar radiation parameterization programs for clear and generalized three-deck cloudy atmospheres for incorporation in the AFGL GCM. For the IR part, high clouds are considered to be nonblack, but middle and low clouds are assumed to be blackbodies. The flux profiles in clear regions separated by clouds and/or the surface are computed based on the same principle used in computing clear atmosphere fluxes. Fluxes within the clouds are determined by interpolation for nonblack clouds and by the blackbody emission for black clouds. For the solar part, there is no distinction between black and nonblack clouds. Instead, cloud radiative properties are obtained based on the prescribed vertical cloud liquid water content. Fluxes between cloud decks are obtained by a ray tracing method, as described in Section 3.

Prediction of cloud cover and cloud configurations is carried out in three steps. First, the cloud cover is computed for each of the model layers designated for cloud formation. Then, by strapping two or more contiguous layers into cloud decks, the cloud cover for each deck is computed based on the averaging scheme. Finally, the total cloud cover is computed by the maximum overlap assumption. There are seven cloud configurations, including three one-deck cases, three two-deck cases, and one one-deck case.

Using five atmospheric profiles, we show that IR clear-sky cooling

rates computed from the present model agree with those obtained from the GFDL/NMC model within about  $0.5^{\circ}\text{K/day}$ . One exception is near the surface, where a difference of about  $2^{\circ}\text{K/day}$  is found for the moist tropical atmosphere. This difference is probably due to different treatments of the water vapor continuum absorption. We have also compared heating rates for various cloudy conditions computed from the present parameterization program with those from a more exact radiative transfer method. This method involves the use of adding/doubling principles and numerous spectral intervals covering solar and IR spectra. We show that the present broadband parameterization program, which is computationally efficient, produces reasonable solar heating and IR cooling rate profiles. We have performed comparisons for atmospheres containing one, two, and three cloud decks. The largest deviation occurs when nonblack and semitransparent high clouds are present.

The present radiation and cloud parameterization program has been successfully incorporated in the AFGL 12-layer GCM. Simulations have been performed for cloud and radiation budget distributions using the initial humidity and temperature fields corresponding to 12Z, 17 June 1979. Zonally averaged global distributions of cloud cover and radiation budgets at the TOA and surface are displayed and examined. Cloud cover and IR and solar fluxes at the TOA are in general agreement with available cloud and radiation budget climatologies. In addition, we also present the zonally averaged atmospheric cooling rate profiles with and without the presence of cloud fields using the AFGL 12-layer GCM. The importance of clouds in the generation of atmospheric cooling is pointed out.

## Appendix A

### SIMPLIFICATION OF RADIATIVE TRANSFER IN HIGH CLOUDS

The upward and downward fluxes below the high cloud in our original program (Liou and Ou, 1981; Liou et al., 1984) are given by

$$F^+(z) = \sigma T_s^4 [1 - \epsilon^f(z, T_s)] + \int_0^z \sigma T^4(z') K(z-z') dz' , \quad (A.1)$$

$$\begin{aligned} F^+(z) &= r^c \{ \sigma T_s^4 [1 - \epsilon^f(2z_b - z, T_s)] + \int_0^z \sigma T^4(z') K(2z_b - z - z') dz' \} \\ &\quad + t_c \{ \int_{z_T}^{z_t} \sigma T^4(z') K(z' - z_t + z_b - z) dz' \} + \epsilon^c \sigma T_b^4 [1 - \epsilon^f(z_b - z, T_b)] \\ &\quad + \int_{z_b}^z \sigma T^4(z') K(z' - z) dz' , \end{aligned} \quad (A.2)$$

where the subscripts *t* and *b* denote the high cloud top and base, respectively. For the region above the high cloud, we have

$$\begin{aligned} F^+(z) &= r^c \int_{z_T}^{z_t} \sigma T^4(z') K(z' + z - 2z_t) dz' + t^c \{ \sigma T_s^4 [1 - \epsilon^f(z - z_t + z_b, T_s)] \\ &\quad + \int_0^{z_b} \sigma T^4(z') K(z - z_t + z_b - z') dz' \} + \epsilon^c \sigma T_t^4 [1 - \epsilon^f(z - z_t, T_t)] \\ &\quad + \int_{z_t}^z \sigma T^4(z') K(z - z') dz' , \end{aligned} \quad (A.3)$$

$$F^+(z) = \int_{z_T}^z \sigma T^4(z') K(z' - z) dz' . \quad (A.4)$$

In Eqs. (A.1)-(A.4) all the notations have been defined in Section 2. As shown in the equations, computations of the broadband flux emissivity become quite involved. To economize the computational effort, we first compute flux components above and below a black cloud at the same position as the high cloud. Thus, below and above the black cloud, we have

$$F_b^+(z) = \sigma T_s^4 [1 - \epsilon^f(z, T_s)] + \int_0^z \sigma T^4(z') K(z-z') dz' , \quad (A.5)$$

$$F_b^-(z) = \sigma T_b^4 [1 - \epsilon^f(z_b-z, T_b)] + \int_{z_b}^z \sigma T^4(z') K(z'-z) dz' , \quad (A.6)$$

$$F_b^+(z) = \sigma T_t^4 [1 - \epsilon^f(z-z_t, T_t)] + \int_{z_t}^z \sigma T^4(z') K(z-z') dz' , \quad (A.7)$$

$$F_b^-(z) = \int_{z_T}^z \sigma T^4(z') K(z'-z) dz' , \quad (A.8)$$

where the subscript b represents the black cloud. For below the high cloud, by substituting Eqs. (A.6) and (A.7) into Eqs. (A.2) and (A.3), respectively, we obtain,

$$\begin{aligned} F^+(z) &= F_b^+(z) + r^c F_r^+(z) + t^c F_t^+(z) \\ &\quad - (1 - \epsilon^c) \sigma T_b^4 [1 - \epsilon^f(z_b-z, T_b)] , \end{aligned} \quad (A.9)$$

and for above the high cloud,

$$\begin{aligned} F^-(z) &= F_b^-(z) + r^c F_r^-(z) + t^c F_t^-(z) \\ &\quad - (1 - \epsilon^c) \sigma T_t^4 [1 - \epsilon^f(z-z_t, T_t)] , \end{aligned} \quad (A.10)$$

where  $r^c F_r^+(z)$ ,  $t^c F_t^+(z)$ ,  $r^c F_r^-(z)$ , and  $t^c F_t^-(z)$  are the reflected and

transmitted flux components below and above the cloud, respectively. We now approximate these four quantities as follows:

$$r^c F_r^{\downarrow}(z) = r^c F^{\uparrow}(z_b) [1 - \epsilon^f(z_b - z, T_b)] , \quad (A.11)$$

$$t^c F_t^{\downarrow}(z) = t^c F^{\uparrow}(z_t) [1 - \epsilon^f(z_b - z, T_b)] , \quad (A.12)$$

$$r^c F_r^{\uparrow}(z) = r^c F^{\uparrow}(z_t) [1 - \epsilon^f(z - z_t, T_t)] , \quad (A.13)$$

$$t^c F_t^{\uparrow}(z) = t^c F^{\uparrow}(z_b) [1 - \epsilon^f(z - z_t, T_t)] , \quad (A.14)$$

where  $F^{\uparrow}(z_t)$  and  $F^{\uparrow}(z_b)$  denote radiative fluxes entering the cloud at the cloud top and bottom, respectively. Substituting Eqs. (A.11)-(A.14) into Eqs. (A.9) and (A.10) and comparing Eqs. (A.5) and (A.8) with Eqs. (A.1) and (A.4), respectively, we obtain, for below the cloud,

$$F^{\uparrow}(z) = F_b^{\uparrow}(z) , \quad (A.15)$$

$$F^{\downarrow}(z) = [r^c F^{\uparrow}(z_b) + t^c F^{\uparrow}(z_t) - (1-\epsilon^c) \sigma T_b^4] [1 - \epsilon^f(z_b - z, T_b)] + F_b^{\downarrow}(z) , \quad (A.16)$$

and for above the cloud,

$$F^{\uparrow}(z) = [r^c F^{\uparrow}(z_t) + t^c F^{\uparrow}(z_b) - (1-\epsilon^c) \sigma T_t^4] [1 - \epsilon^f(z - z_t, T_t)] + F_b^{\uparrow}(z) , \quad (A.17)$$

$$F^{\downarrow}(z) = F_b^{\downarrow}(z) . \quad (A.18)$$

The above modification replaces complicated and redundant computations of the transmitted and reflected fluxes with one-time calculations of input fluxes at the cloud boundary, and thus reduces the computation time by one half. The resulting radiative heating rate and flux profiles from this modified scheme differ from those in the original scheme by a negligible amount.

Appendix B  
DOCUMENTATION OF RADIATION PARAMETERIZATION  
PROGRAMS

B.1 General Description of the Program

The basic principles for calculating both IR and solar radiation fluxes and heating rates have been described in Sections 2 and 3. Here, we document detailed computer routines for IR and solar parameterization programs for use in general circulation models.

The entire radiation program is composed of three subroutines denoted as PRERAD, IRRAD, and IRCLR. The subroutine PRERAD serves as a driver program that connects the main part of radiation calculations with other GCM programs. It interpolates the model-generated temperature and humidity profiles from the main part of the GCM on layers designed for radiation calculations. The cloud position, along with cloud cover and thickness, are determined and used as input to the subroutine IRRAD, which is subsequently called. The computed radiative heating rates for radiation layers from the subroutine IRRAD are then weighted by density to get the mean radiative heating rate for each GCM layer.

The subroutine IRRAD is the main program for radiation calculations. It is composed of IR and solar parts. In the IR part, the path lengths in pressure coordinates are first computed and then adjusted in accordance with a number of temperature and pressure correction schemes denoted in Section 2. Next, the coefficients of the third-order polynomial for IR emissivities are obtained by interpolation between the

prescribed reference temperatures listed in Table 1. The IR program is then connected to a large computational loop in which radiative fluxes for each cloud configuration are calculated. The strategy for computing fluxes has been illustrated in Fig. 3. For computing fluxes in a clear atmosphere, the subroutine IRCLR is called with the lower and upper boundaries being the surface and top of the atmosphere, respectively.

For computing fluxes above and below a high cloud deck, we first obtain the flux profiles for both above and below the cloud by calling the subroutine IRCLR, assuming that the cloud is a blackbody. Then the fluxes are adjusted to account for the effect of transmission through and reflection by the high cloud, according to Eqs. (A.10)-(A.13). On the other hand, fluxes above a black cloud without an overhead high cloud, or between two black clouds, or below a black cloud are obtained by calling IRCLR. Intracloud flux profiles are obtained either by interpolation (high cloud) or by the blackbody assumption (middle and low clouds).

The solar program can be divided into three parts. First, the path lengths of each model layer for  $H_2O$ ,  $CO_2$ , and  $O_3$  are computed. These layered path lengths are then substituted into equations for the computation of gaseous absorptivities. Second, fluxes for the clear sky are obtained. Third, the computation of cloudy sky fluxes is further divided into three parts, according to the number of cloud decks involved. The first part consists of computing the cloud optical properties based on the input cloud thickness and prescribed cloud water content. In the event that there is only one cloud deck, the flux computation is carried out based on the ray tracing principle. The other two parts consist of computing two- and three-deck fluxes, according to the methods described

in Section 3.

Finally, the subroutine IRCLR computes IR fluxes in clear regions. It can be used to compute the entire clear column between the model top and surface, the clear region between the low and middle clouds, as well as between these clouds and the surface. To carry out the flux integration for clear columns the flux equation is generalized in the following finite-difference form

$$F_{im} = E_i (1 - \epsilon_{im,k}^f) + \sum_{j=n_s}^{n_e} \bar{E}_{j+1/2} (\epsilon_{im,j}^f - \epsilon_{im,j-1}^f) S_1 , \quad (B.1)$$

where

$$\bar{E}_{j+1/2} = \sigma T_{j+1/2}^4 , \quad (B.2)$$

$S_1$  is the sign parameter,  $\epsilon_{im,j}^f$  represents the flux emissivity for the slab layer between levels  $m$  and  $j$  for the  $i$ th flux component, and  $F_{im}$  is the  $i$ th flux component at level  $m$ , so that

$$F_{1m} = F_m^+ ,$$

$$F_{2m} = F_m^- .$$

Table B.1 gives the respective parameters involved in Eq. (B.1).

## B.2 Interfacing with the AFGL GCM

A schematic flow diagram illustrating the connection between the AFGL GCM and the radiation program is depicted in Fig. B.1. In the AFGL GCM main program the subroutine LALOOP is called to compute large-scale parameters for a specific time step. The subroutine NLPROD is called in

Table B.1 Assignments of parameters involved in Eq. (B.1).

i	$n_s$	$n_e$	k	$s_i$	$E_i$
1	$m_b + 1$	$m$	$m_b$	-1	$\sigma T_b^4$
2	$m + 1$	$m_t$	$m_t$	1	$\sigma T_t^4$
$m_b$ :	level index for the base of the integration domain				
$m_t$ :	level index for the top of the integration domain				
$T_b$ :	temperature at the base of the integration domain				
$T_t$ :	temperature at the top of the integration domain				

LALOOP to compute the nonlinear product in LALOOP. In NLPROD, the subroutine SUBRAD is called to compute radiative transfer parameters. In the subroutine SUBRAD, the solar zenith angles are computed through the subroutine ZENITH, the cloud cover field is computed through the subroutine CLOUD, and then the subroutine PRERAD is called to compute the radiative heating rate, which is subsequently added to the large-scale heating rate previously computed in NLPROD. The vertical grid structure used in radiation routines is consistent with the AFGL GCM grid structure, so that there is no vertical interpolation of the large-scale parameters required in the radiation routine and computation time is saved. The effects of the vertical resolution have been shown in Section 4 through the intercomparison of clear and cloudy heating rate profiles.

Another link between the AFGL GCM and radiative routines is the computation of the surface radiative flux balance. The downward IR flux and downward net solar flux at the surface for each grid are generated in radiative routines and transferred to the AFGL GCM through the common block VARIA, for computing the surface energy balance in the routines for

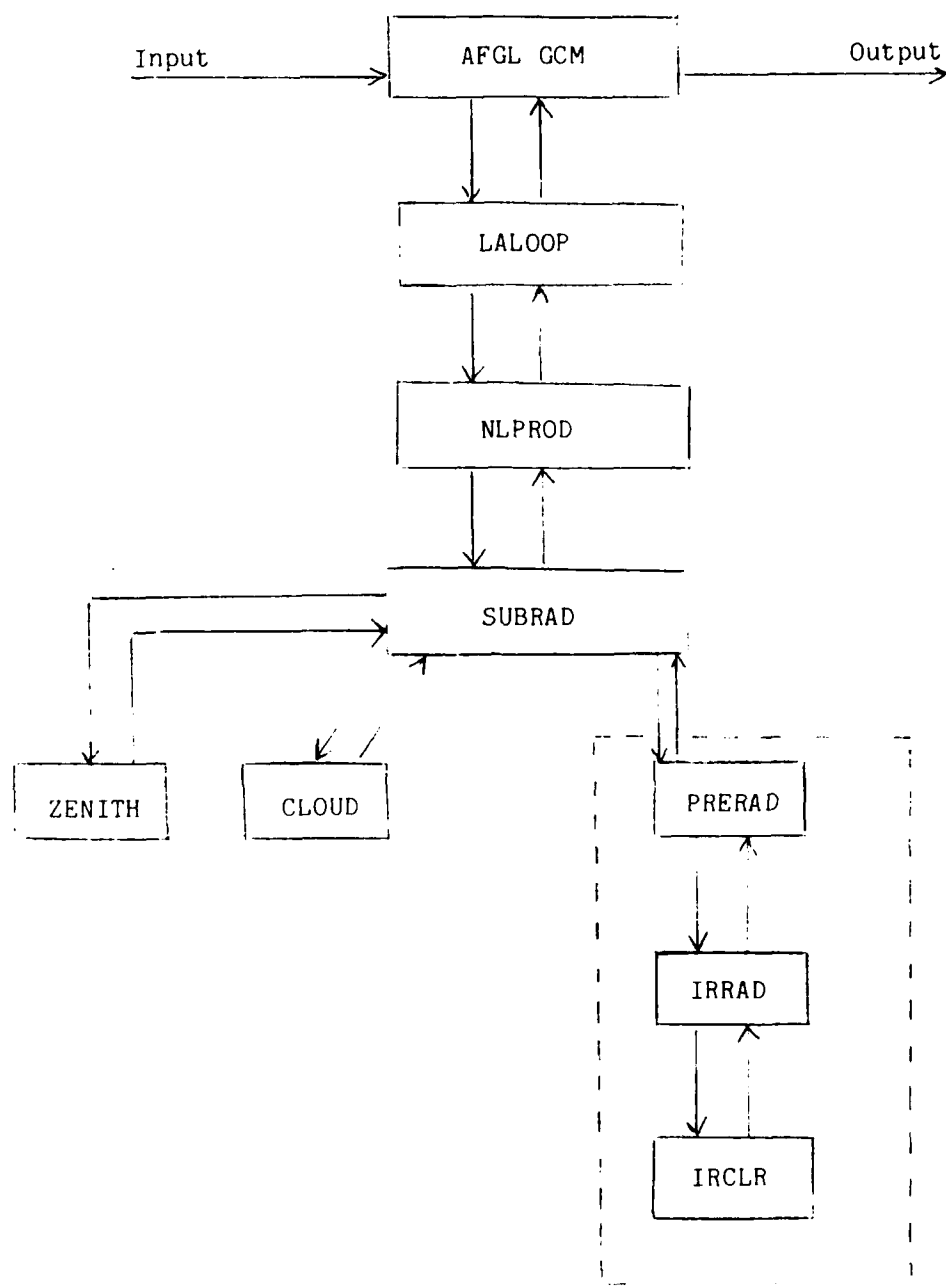


Fig. B.1 A schematic flow diagram illustrating the interface of the AFGL GCM with the current radiation programs. The routines contained in the dashed lines are radiation routines.

boundary layer fluxes.

### B.3 Changes Required in the Radiative Routines for Converting Variable Resolution to Fixed Resolution

The radiative routines have been modified to accomodate computations using variable vertical resolutions, since a variable-resolution version of the AFGL GCM is already available. Every time the variable-resolution radiative routines are converted to the fixed-resolution version, certain changes must be made. These changes can be divided into three groups as follows:

- 1) The common blocks transfer parameters between the AFGL GCM and radiative routines: these common blocks include CCONST, GRDPT, ALEG, SURFAC, VRTST, BL, CZALB, STORE and BLFXT. The specifications of array dimensions need to be changed so as to be consistent with the AFGL GCM.
- 2) The DATA statements assign values to JUDGE arrays: JUDGE (J,K) is a 2-dimensional array. It is introduced to the program for prescribing cloud top and base level indices and cloud types. The level indices are used in radiative routines to specify clear regions separated by clouds. The cloud types are required information for computing the solar radiative properties of clouds. The first argument J indicates the cloud configuration. The high, middle, and low cloud decks are given indices of 1, 2, and 3, respectively, whenever that cloud deck is present in the grid. If no cloud deck is present, the index is zero. Then the value of J is obtained by

$$J = \sum_{j=1}^3 [I(j)]^2 , \quad (B.3)$$

where  $I(j)$  is the index for the  $j$ th cloud deck. The second argument  $K$  denotes the cloud top ( $K = 1, 4, 7$ ) and base ( $K = 2, 5, 8$ ) level indices, and the cloud type ( $K = 3, 6, 9$ ). For a two-deck (high and low clouds) case,

$$J = 1 + 9 = 10$$

JUDGE (10,1) is the high cloud top level index, JUDGE (10,2) the high cloud base level index, JUDGE (10,3) the high cloud type index, JUDGE (10,4) the low cloud top level index, JUDGE (10,5) the low cloud base level index, JUDGE (10,6) the low cloud type index, and JUDGE (10,7) = JUDGE (10,8) = JUDGE (10,9) = 0. These quantities of JUDGE need to be respecified every time the vertical resolutions are changed.

3) The DATA statements assign humidity and ozone mixing ratios: the variable E1 is the humidity mixing ratio. The AFGL GCM only provides humidity values up to a certain sigma value (usually corresponding to the tropopause). Thus the humidity mixing ratio in the stratosphere needs to be respecified, according to climatology, when the vertical resolution is changed. The variable Q1 is the ozone mixing ratio. Since the AFGL GCM does not provide the ozone mixing ratio, this quantity also needs to be prescribed over the whole vertical column according to the climatological mean. Finally, the quantity LTOP, which denotes the top level index for the Rayleigh reflecting layer, needs to be changed.

Appendix C  
 DIRECTORY OF ARRAYS AND VARIABLES IN  
 THE RADIATIVE ROUTINES

A. Subroutine PRERAD

1. Atmospheric properties

<u>Array</u>	<u>Meaning</u>
CL9 (8)	sigma structure array
E1 (40)	layer humidity mixing ratio
Q1 (40)	layer ozone mixing ratio
T1 (40)	layer temperature
PTX (6)	surface pressure and temperature
W (96,2,12)	humidity field (longitude • sigma) for two equator-symmetric latitude circles from the GCM
T (96,2,12)	temperature field (longitude • sigma) for two equator-symmetric latitude circles from the GCM
SL (12)	layer sigma values from the GCM
T0 (12)	reference temperature

<u>Variable</u>	<u>Meaning</u>
HBAR	prescribed relative humidity in the stratosphere
HQ <sub>s</sub>	saturated humidity mixing ratio in the stratosphere

2. Storage arrays

<u>Array</u>	<u>Meaning</u>
FNIR (96,76)	net upward IR flux field at the surface
FNSOL (96,76)	net downward solar flux field at the surface
KFLUX (96,76,9)	storage array for IR, solar, and net fluxes at the top of the atmosphere, within the atmosphere and the surface
RIIR (96,2,13)	IR radiative heating rate for two equator-symmetric latitude circles
RISOL (96,2,13)	solar radiative heating rate for two equator-symmetric latitude circles
IFLUX (76,9)	storage array for zonally averaged IR, solar, and net flux fields

### 3. Radiative parameters

<u>Array</u>	<u>Meaning</u>
H9 (4)	solar heating rate
H (40)	IR heating rate
RIRAD (96,2,13)	net radiative heating (longitude • sigma) for two equator-symmetric latitude circles
SZ (96,2)	cosine of the solar zenith angle field
SALB (96,2)	surface albedo field

<u>Variable</u>	<u>Meaning</u>
UIRF	net upward IR flux at the surface
DIRF	downward IR flux at the surface
CZ	cosine of the solar zenith angle for one grid point
SA	surface albedo for one grid point
DSOLF	downward solar flux at the surface

### 4. Cloud parameters

<u>Array</u>	<u>Meaning</u>
CB (7,3)	cloud deck base level sigma
CT (7,3)	cloud deck top level sigma
FRACT (7)	cloud cover
ICL (96,76,4)	cloud cover field in decades of percentage
L23 (6,7)	cloud deck top and base level indices
JUDGE (14,9)	reference array storing cloud deck top and base level indices and cloud type index for all configurations
LTYPE (7,3)	cloud type index

<u>Variable</u>	<u>Meaning</u>
LCBOT	high cloud base level index
LCTOP	high cloud top level index
IFRACT	cloud cover for one grid point in decades of percentage
ISUM	sum of square of cloud deck indices

### 5. Constants

<u>Array</u>	<u>Meaning</u>
PHI (76)	grid point latitude value
LNGTD (96)	grid point longitude value
GLAT (38)	Gaussian latitude values

5. Constants (cont.)

<u>Variable</u>	<u>Meaning</u>
SECPDY	seconds per day
SIG	Stefan-Boltzman constant
PII	$\pi$
NCLD	total number of cloud configurations (including clear case) in a grid
NCLDM	NCLD - 1
NGCM	total number of GCM model levels
MP	total number of GCM longitudinal grids
NP	total number of GCM latitudinal grids
NP2	NP/2
NP2P	NP2 + 1
KP	total number of GCM vertical grids
KPHL	total number of humidity data void layers + 1
KPM1	KP - 1
KPP1	KP + 1
LTOP	level index for the top of the Rayleigh scattering layer

B. Subroutine IRRAD

1. Atmospheric properties

<u>Arrays</u>	<u>Meaning</u>
PRM (40)	model level pressure
TEM (40)	model level temperature
AVGQ (40)	model level humidity
F (5, 40)	pressure and temperature scaling factor
URF (5, 40)	pressure and temperature scaled path
UWCOM (6, 40)	unscaled path
PTX (6)	surface pressure and temperature
T1 (40)	layer temperature from MAIN
E1 (40)	layer humidity mixing ratio from MAIN
Q1 (40)	layer ozone mixing ratio from MAIN
CL9 (80)	sigma structure array
PBL (40)	model level pressure
PBY (40)	model layer pressure
PBD (40)	model layer pressure thickness
PMD (40)	mean scaled pressure (counted +)
PMU (40)	mean scaled pressure (counted +)
VPY (40)	model layer H <sub>2</sub> O path thickness
OPY (40)	model layer O <sub>3</sub> path thickness
CPY (40)	model layer CO <sub>2</sub> path thickness
VDS (40)	integrated path for H <sub>2</sub> O (downward)
ODS (40)	integrated path for O <sub>3</sub> (downward)

1. Atmospheric properties (cont.)

<u>Arrays</u>	<u>Meaning</u>
CDS (40)	integrated path for CO <sub>2</sub> (downward)
VUS (40)	integrated path for H <sub>2</sub> O (upward)
OUS (40)	integrated path for O <sub>3</sub> (upward)
CUS (40)	integrated path for CO <sub>2</sub> (upward)
<u>Variables</u>	<u>Meaning</u>
PDN	$\int u_w dp_w$ , p <sub>w</sub> : water path
VDN	$\int dp_w$

2. IR gaseous radiative properties

<u>Arrays</u>	<u>Meaning</u>
ABSB (40,2,6)	emissivity between the surface and level of interest
REFT (4)	reference temperature for determining emissivity
RK (5,40)	reference emissivity for path lengths less than 10 <sup>-7</sup> g cm <sup>-2</sup>
RJ (5,40,4)	temperature-interpolated emissivity coefficients
EE (5,4,4)	broadband emissivity coefficients for five bands and four temperatures
INDEXT (40)	reference temperature index for each model level
DT (40)	interpolation factor for temperature
CDT (40)	1 - DT
<u>Variable</u>	<u>Meaning</u>
INMN	INDEX(M) + 1

3. Solar gaseous radiative properties

<u>Arrays</u>	<u>Meaning</u>
WVA (40)	$\int A_v dv$ for downward direct solar radiation in 2.7 $\mu\text{m}$ band
WVB (40)	$\int A_v dv$ for downward diffuse solar radiation in 2.7 $\mu\text{m}$ band
WVC (40)	$\int A_v dv$ for upward diffuse solar radiation in 2.7 $\mu\text{m}$ band
WEI (40)	weighting factor $\epsilon$ for downward direct solar radiation in 2.7 $\mu\text{m}$ band
WEJ (40)	$\epsilon$ for downward diffuse solar radiation in 2.7 $\mu\text{m}$ band

### 3. Solar gaseous radiative properties (cont.)

<u>Arrays</u>	<u>Meaning</u>
WEK (40)	$\epsilon$ for upward diffuse solar radiation in 2.7 $\mu\text{m}$ band
BLS (7)	$\Delta v$
CLS (7)	C-factor
DLS (7)	D-factor
ELS (7)	K/D-factor
FLS (7)	fraction of $\text{H}_2\text{O}$ bands
FOZ (18)	fraction of $\text{O}_3$ bands
AOZ (18)	$\text{O}_3$ absorption coefficients
ACD (40)	$\text{CO}_2$ absorption (downward direct)
ACY (40)	$\text{CO}_2$ absorption (downward diffuse)
ACU (40)	$\text{CO}_2$ absorption (upward diffuse)
AVD (6,40)	$\text{H}_2\text{O}$ absorption (downward direct)
AVY (6,40)	$\text{H}_2\text{O}$ absorption (downward diffuse)
AVU (6,40)	$\text{H}_2\text{O}$ absorption (upward diffuse)
ABD (40)	broadband absorption for $\text{H}_2\text{O} + \text{O}_3$ (downward direct)
ABY (40)	broadband absorption for $\text{H}_2\text{O} + \text{O}_3$ (downward diffuse)
ABU (40)	broadband absorption for $\text{H}_2\text{O} + \text{O}_3$ (upward diffuse)
AAD (40)	broadband absorption for $\text{H}_2\text{O}$ (downward direct)
AAY (40)	broadband absorption for $\text{H}_2\text{O}$ (downward diffuse)
AAU (40)	broadband absorption for $\text{H}_2\text{O}$ (upward diffuse)
AOU (40)	broadband absorption for $\text{O}_3$ (upward diffuse)
AO <sub>1</sub> (40)	broadband absorption for $\text{O}_3$ (downward diffuse)
AOD (40)	broadband absorption for $\text{O}_3$ (downward direct)
AUX (6)	constants for converting scaled path to logarithmic path
AUX (6)	constants for converting scaled path to logarithmic path
<u>Variables</u>	<u>Meaning</u>
X0	$10^{\text{C/D}}$
ADD2	$1 - A^+(z_{t1})$
ADD3	$1 - A^+(z_{t2})$
ADD4	$1 - A^+(z_{t3})$
AUU1	$1 - \bar{A}^+(z_{t1})$
AUU2	$1 - \bar{A}^+(z_{t2})$
AUU3	$1 - \bar{A}^+(z_{t3})$
AYY2	$1 - \bar{A}^+(z_{t1})$
AYY3	$1 - \bar{A}^+(z_{t2})$
AYY4	$1 - \bar{A}^+(z_{t3})$

4. IR cloud radiative properties

<u>Arrays</u>	<u>Meaning</u>
YRE (6)	coefficients for high cloud IR reflectivity
YTR (6)	coefficients for high cloud IR transmissivity
YEM (6)	coefficients for high cloud IR emissivity
<u>Variables</u>	<u>Meaning</u>
EC	high cloud IR emissivity
RR	high cloud IR reflectivity
TT	high cloud IR transmissivity

5. Solar cloud radiative properties

<u>Arrays</u>	<u>Meaning</u>
Y (8,44)	coefficients for solar cloud radiative properties
YT (8,3,3)	coefficients for solar cloud radiative property with temperature adjustments
YA (4,4,4)	coefficients for solar cloud absorption properties
TREF (4)	reference temperature for computing temperature adjustment for each type of cloud
RC (2)	direct solar cloud reflectivity for 1- or 2-layer clouds
TC (2)	direct solar cloud transmissivity for 1- or 2-layer clouds
RCBAR (2)	diffuse solar cloud reflectivity for 1- or 2-layer clouds
TCBAR (2)	diffuse solar cloud transmissivity for 1- or 2-layer clouds
ACBAR (2)	diffuse solar cloud absorptivity for 1- or 2-layer clouds
AC (2)	direct solar cloud absorptivity for 1- or 2-layer clouds
WREF (4)	maximum cloud liquid water content
<u>Variables</u>	<u>Meaning</u>
TTTT	cloud transmittance
RRRR	cloud reflectance
AAAA	cloud absorption
AAA	absorptivity a
RRR	reflectivity r
TTT	transmissivity t

5. Solar cloud radiative properties (cont.)

<u>Variables</u>	<u>Meaning</u>
RCTC	$r + t + a$
RCL	normalized $r$
TCL	normalized $t$
RUO	normalized $r$
TUO	normalized $t$
RCBR1	$RCBAR(1)/RCTC1$
RCBR2	$RCBAR(2)/RCTC2$
RCL1	$RC(1)/RCTC1$
RCL2	$RC(2)/RCTC2$
RCTC1	$r_1^c + t_1^c + a_1^c$
RCTC2	$r_2^c + t_2^c + a_2^c$
RTBR	$\bar{r}_k^c + \bar{t}_k^c + \bar{a}_k^c$
TCBR1	$TCBAR(1)/RCTC1$
TCBR2	$TCBAR(2)/RCTC2$
TCL1	$TC(1)/RCTC1$
TCL2	$TC(2)/RCTC1$

6. IR radiative transfer quantities

<u>Arrays</u>	<u>Meaning</u>
ST (8,40)	components of radiative flux for various cloud types plus weighted average
NX (4)	index for components above high cloud
NCHAN (8,3)	flag matrix for variable INDD elements (1 = variable)
AT (40)	$T_1^4$ (layer temperature)
SS (6,40)	Components of radiative fluxes for one band
TQD (8)	$T_s^4$ ( $T_s$ : surface temperature)
SGN (8)	prefix matrix
AUX (6)	constants for converting scaled path to logarithmic path
AUY (6)	
H (80,40)	IR cooling rate vector
<u>Variables</u>	<u>Meaning</u>
W1 } W2 }	linear interpolation factor for in-cloud radiative fluxes
DFLUX	$(1-\epsilon^c) [F^4(z_t) - \sigma T_b^4] + r^c F^4(z_b)$ [Eqs. (A.16), (A.17)]
DIRF	downward IR flux at the surface
UIRF	net upward IR flux at the surface

## 7. Solar radiative transfer quantities

<u>Arrays</u>	<u>Meaning</u>
H9 (40)	solar heating rate
FDS (40)	downward solar flux
FUS (40)	upward solar flux
<u>Variables</u>	<u>Meaning</u>
CZ	solar zenith angle $\mu_0$
SA	solar surface albedo $r_s$
ANGLE	solar zenith angle $\mu_0$
SOLAR	solar constant $S_0$
ALB	solar surface albedo $r_s$
EINSO	$S_0 \mu_0$
RAS	Rayleigh layer reflectance (diffuse)
RAL	Rayleigh layer reflectance (direct)
REF	total atmospheric Rayleigh layer reflectance
FZT	downward flux at the top of Rayleigh layer
FZBU	upward flux at the cloud base
T	$1 - [ABD(\text{layer}) - ABD(\text{LBUP})]/[1 - ABD(\text{LBUP})]$
TD	$1 - [ABY(\text{layer}) - ABY(\text{LBUP})]/[1 - ABD(\text{LBUP})]$
TU	$1 - ABU(\text{LBCL})$
S12	$\bar{S}_{12}$
S23	$\bar{S}_{23}$
S34	$\bar{S}_{34}$
AXX	$1 - ABU(\text{LTCL})$
AYY	$1 - ABD(\text{LBUP})$
DSOLF	downward net solar flux at the surface
G1D	$G_1^+$
G2D	$G_2^+$
G3D	$G_3^+$
G4D	$G_4^+$
G1U	$\bar{G}_1^+$
G2U	$\bar{G}_2^+$
G3U	$\bar{G}_3^+$
G4U	$\bar{G}_4^+$
G1Y	$G_1^+$
G2Y	$\bar{G}_2^+$
G3Y	$\bar{G}_3^+$
G4Y	$\bar{G}_4^+$
XG1	$x_1$
XG2	$x_2$
YG1	$y_1$
YG2	$y_2$
YG3	$y_3$

7. Solar radiative transfer quantities (cont.)

<u>Variables</u>	<u>Meaning</u>
YG4	$y_4$
TOD	$T_0^+$
T1D	$T_1^+$
T2D	$T_2^+$
T3D	$T_3^+$
T1U	$\bar{T}_1^+$
T2U	$\bar{T}_2^+$
T3U	$\bar{T}_3^+$
T1Y	$\bar{T}_1^+$
T2Y	$\bar{T}_2^+$
T3Y	$\bar{T}_3^+$

8. Cloud properties

<u>Arrays</u>	<u>Meaning</u>
LC (6)	cloud top and cloud base level indices (counted top +)
NLC (6)	cloud top and cloud base level indices (counted bottom +)
L23 (6,7)	cloud top and base level index (top +)
FRACT (7)	cloud fraction
THK	cloud thickness
WTCNT (6,7,3)	liquid water content for different types of clouds
LTYPE (7,3)	cloud type index

<u>Variables</u>	<u>Meaning</u>
ISUM	summation of square of cloud deck index, first argument of JUDGE
LCTOP	cirrus cloud-top index (+)
LCBOT	cirrus cloud-base index (+)
WZ	total liquid water path
PART	cloud fraction
LTCL	cloud top index
LBCL	cloud base index
DZ	cloud thickness
IC	cloud type index
AGT	average temperature in cloud
ICX	(cloud type index) * 2-1
ICY	(cloud type index) * 2
LTUP	LTCL - 1
LBDN	LBCL + 1
LTDN	LTCL + 1
LBUP	LBCL - 1
LTUP1	LC(1) - 1

## 8. Cloud properties (cont.)

<u>Variables</u>	<u>Meaning</u>
LTUP2	LC(3) - 1
LTUP3	LC(5) - 1
LBDN1	LC(2) + 1
LBDN2	LC(4) + 1
LBDN3	LC(6) + 1
LTCL1	LC(1)
LTCL2	LC(3)
LTCL3	LC(5)
LBCL1	LC(2)
LBCL2	LC(4)
LBCL3	LC(6)
LBUP1	LC(2) - 1
LBUP2	LC(4) - 1
LBUP3	LC(6) - 1
LTDN1	LC(1) + 1
LTDN2	LC(3) + 1
LTDN3	LC(5) + 1
NMM	NLC(1) - 1
NPP	NLC(2) + 1

## 9. Constants

<u>Variables</u>	<u>Meaning</u>
LEVEL	total number of model levels
NLYR	total number of model layers
NCLD	total number of cloud types
LTOP	index for the top level of Rayleigh's reflection layer
SIG	Stefan-Boltzmann constant
CPR	constant for computing reduced CO <sub>2</sub> path
NLVL	total number of model levels
NTOT	total number of non-overlap bands
NTOTAL	total number of bands
LSRFC	surface or cloud top level index below the high cloud
NCLDP	total cloud type number + 1
LAYER	total number of model layers
LAYERM	LAYER - 1
CP	specific heat at constant pressure for air
IFLG	flag for printing radiative transfer quantities
KKE	number of cloud decks

### C. Subroutine IRCLR

#### 1. Atmospheric variables

<u>Arrays</u>	<u>Meaning</u>
UPATH (6,40)	path length between emission and contributing levels
URF (5,40)	path length
AT (40)	T <sup>4</sup> (layer temperature)
UWCOM (6,40)	unadjusted path length
TEM (40)	model level temperature

#### 2. Radiative Variables

<u>Arrays</u>	<u>Meaning</u>
ABSB (40,2,6)	emissivity between surface and level of interest
EMMI (6,40)	emissivity corresponding to UPATH
FLUXI (6,6,40)	components of fluxes
SS (6,40)	components of fluxes
DRK (4)	$a_1 u^{1-1}$ (emissivity term)
DEMIS (6)	$1 - \epsilon^f(u, T_s)$ or $\epsilon^f(u + \Delta u, T) - \epsilon^f(u, T)$
RK (5,40)	reference emissivity for path lengths less than $10^{-7} \text{ g cm}^{-2}$
RJ (5,40,4)	temperature-interpolated emissivity coefficients
INDD (8,4)	prefix and indice matrix
TQD (8)	T <sup>4</sup> (T <sub>s</sub> : surface temperature)
NCHAN (8, 3)	flag matrix for variable INDD elements 1 = variable)
SCM (8)	prefix matrix
AUX (6)	constants for converting scaled path to logarithmic path
AUY (6)	

#### 3. Constants

<u>Variables</u>	<u>Meaning</u>
SIG	$\sigma$ : Stefan-Boltzmann constants
CPR	constants for computing CO <sub>2</sub> path
NLVL	total number of model levels
NTOT	total number of non-overlap bands
NTOTAL	total number of bands
LEVB	level index of clear region base
LEVT	level index of clear region top
NNS	emission level index
NNE	contributing level index
NN3	some reference index
NN4	boundary index
NNSP	NNS + 1

## REFERENCES

Chou, M.D. and A. Arking, 1980: Computation of infrared cooling rates in the water vapor bands. J. Atmos. Sci., 37, 855-867.

Cox, S.K., 1969: Observational evidence of anomalous infrared cooling in a clear tropical atmosphere. J. Atmos. Sci., 26, 1347-1349.

Deirmendjian, D., 1969: Electromagnetic Scattering on Spherical Polydispersions. Elsevier, New York, 290 pp.

Downing, H.D. and D. Williams, 1975: Optical constants of water in the infrared. J. Geophys. Res., 80, 1656-1661.

Fels, S.B. and M.D. Schwarzkopf, 1981: An efficient, accurate algorithm for calculating CO<sub>2</sub> 15 μm band cooling rates. J. Geophys. Res., 86, 1205-1232.

Geleyn, J.F., 1981: Some diagnostics of the cloud/radiation interaction in ECMWF forecast model. In Proceedings of Workshop on Radiation and Cloud-Radiation Interaction in Numerical Modeling, ECMWF, Reading, England, 135-162.

Goldman, A. and T.G. Kyle, 1968: A comparison between statistical model and line-by-line calculation with application to the 9.6 μm and 2.7 μm water vapor bands. Appl. Opt., 7, 1167-1177.

Hemming, R.W., 1973: Numerical Methods for Scientists and Engineers. 2nd Edition, McGraw-Hill, New York, 721 pp.

Heymsfield, A.J., 1975: Cirrus uncinus generating cells and the evolution of cirroform clouds. J. Atmos. Sci., 32, 799-808.

Howard, J.N., D.L. Burch and D. Williams, 1956: Near infrared transmission through synthetic atmospheres. J. Opt. Soc. Amer., 46, 186-190.

Inn, E.C. and Y. Tanaka, 1953: Absorption coefficient of ozone in the ultraviolet and visible regions. J. Opt. Soc. Amer., 43, 870-873.

Kinne, S., 1987: Parameterization of radiative transfer in the earth's atmosphere with specific applications to clouds. Ph.D. dissertation, University of Utah, 108 pp.

Koenig, G., K.N. Liou and M. Griffin, 1987: An investigation of cloud/radiation interactions using three-dimensional nephanalysis and earth radiation budget data bases. J. Geophys. Res., 92, 5540-5554.

Lacis, A.A. and J.E. Hansen, 1974: A parameterization for the absorption of solar radiation in the earth's atmosphere. J. Atmos. Sci., 31, 118-133.

Liou, K.N., 1980: An Introduction to Atmospheric Radiation. Academic Press, New York, 392 pp.

Liou, K.N. and S.C. Ou, 1981: Parameterization of infrared radiative transfer in cloudy atmospheres. J. Atmos. Sci., 38, 2707-2716.

Liou, K.N. and S.C. Ou, 1983: Theory of equilibrium temperature in radiative-turbulent atmospheres. J. Atmos. Sci., 40, 214-229.

Liou, K.N., S.C. Ou, S. Kinne and G. Koenig, 1984: Radiation parameterization programs for use in general circulation models. Report AFGL-TR-84-0217, ADA148015, Air Force Geophysics Laboratory, Hanscom AFB, MA, 53 pp.

Liou, K.N. and T. Sasamori, 1975: On the transfer of solar radiation in aerosol atmospheres. J. Atmos. Sci., 32, 2166-2177.

Liou, K.N. and C.D. Wittman, 1979: Parameterization of the radiative properties of clouds. J. Atmos. Sci., 36, 1261-1273.

London, J., 1957: A study of the atmospheric heat balance. New York University, Final Report, Contract AF19(122)-166, 99 pp.

McClatchey, R.A., R.W. Fenn, J.E.A. Selby, F.E. Volz and J.S. Gaming, 1971: Optical properties in the atmosphere. Environmental Research Paper, No. 354, AFCRL-71-0279, AD726116, 81 pp.

Mason, B.J., 1971: The Physics of Clouds. 2nd Edition, Clarendon Press, 671 pp.

Ou, S.C. and K.N. Liou, 1983: Parameterization of carbon dioxide 15  $\mu\text{m}$  absorption and emission. J. Geophys. Res., 88, 5203-5207.

Plass, G.N., G.W. Kattawar and F.E. Catchings, 1973: Matrix-operator theory of radiative transfer. Appl. Opt., 12, 314-329.

Roberts, R.E., J.A. Selby and L.M. Biblerman, 1976: Infrared continuum absorption by atmospheric water vapor in the 8-12  $\mu\text{m}$  window. Appl. Opt., 15, 2085-2090.

Rodgers, C.D. and C.D. Walshaw, 1966: The computation of infrared cooling in planetary atmospheres. Quart J. Roy. Meteor. Soc., 92, 67-92.

Roewe, D. and K.N. Liou, 1978: Influence of cirrus clouds on the infrared cooling rate in the troposphere and lower stratosphere. J. Appl. Meteor., 17, 92-106.

Rothman, L.S., R.R. Gamache, A. Barbe, A. Goldman, J.R. Gillis, L.R. Brown, R.A. Toth, J.M. Flaud and C. Camy-Peyret, 1983: AFGL atmospheric line parameters compilation: 1982 edition. Appl. Opt., 22, 2247-2256.

Schaaf, J.W. and D. Williams, 1973: Optical properties of ice in the infrared. J. Opt. Soc. Amer., 63, 726-732.

Slingo, J. and B. Ritter, 1984: Cloud prediction in the ECMWF model.  
ECMWF Technical Report No. 46, Reading, England, 49 pp.

Stephens, G.L., G.G. Campbell and T.H. Vonder Haar, 1981: Earth  
radiation budgets. J. Geophys. Res., 86, 9739-9760.

Vigroux, E., 1953: Contributions a l'étude experimentale de absorption  
de l'ozone. Ann. Phys., 8, 709-762.

END  
DATE  
FILED  
DTIC

JULY 88